

Test of the cosmological principle by means of CMB multipole vectors for $l \leq 50$

Marvin Pinkwart^{1,2,*} and Dominik J. Schwarz^{1,†}

¹*Fakultät für Physik, Universität Bielefeld, Postfach 100131, 33501 Bielefeld, Germany*

²*Department of Physics and Earth Sciences, Jacobs University Bremen, Campus Ring 1, 28759 Bremen, Germany*

(Dated: July 5, 2022)

The statistical cosmological principle states that observables on the celestial sphere are sampled from a rotationally invariant distribution. Previously certain large scale anomalies which violate this principle have been found, for example an alignment of the lowest multipoles with the cosmic dipole direction. In this work we continue the investigation of possible violations of statistical isotropy using multipole vectors which represent a convenient tool for this purpose.

We investigate all four full-sky foreground-cleaned maps from the Planck 2015 release with respect to four meaningful physical directions using computationally cheap statistics that have a simple geometric interpretation. We find that the SEVEM map deviates strongly from all the other cleaned maps and should not be used for cosmological full-sky analyses of statistical isotropy. The other three maps COMMANDER, NILC and SMICA show a remarkably consistent behavior. On the largest angular scales, $l \leq 5$, as well as on intermediate scales, $l = 20, 21, 22, 23, 24$, all of them are unusually correlated with the cosmic dipole direction. These scales coincide with the scales on which the angular power spectrum deviates from the Planck 2015 best-fit Λ CDM model. In the range $2 \leq l \leq 50$ as a whole there is no unusual behavior visible globally. We do not find abnormal intra-multipole correlation, i.e. correlation of multipole vectors inside a given multipole without reference to any outer direction, but we observe a lack of variance in intra-multipole alignment statistics.

The possibility of a connection between galactic center foreground and previously reported parity anomalies is discussed.

PACS numbers: 02.50.Cw, 02.70.Uu, 07.05.Kf, 98.80.Es

Keywords: cosmic microwave background – data analysis – multipole vectors – statistical isotropy

I. INTRODUCTION

High-fidelity observations of the cosmic microwave background (CMB) at the largest angular scales became available with the release of the data from the Wilkinson Microwave Anisotropy Probe (WMAP) [1]. Previous full-sky analyses based on data from the Cosmic Background Explorer (COBE) suffered at the largest angular scales from their limited capacity (only three frequency bands) to reliably separate the various foreground components from the CMB. Once confidence on foreground separation techniques was built, the WMAP data offered the potential to address the statistical isotropy of the observed temperature anisotropies at large scales. It was noted that the quadrupole and octopole seem to be aligned with each other [2, 3] and with the CMB dipole [3] and an unexpected hemispherical asymmetry was revealed [4]. More signs of violation of statistical isotropy have been found in several publications [5–12].

On the other hand, already the WMAP data suggested that deviations from Gaussianity and from the angular power spectrum predicted by the Λ CDM model are negligibly small [13, 14]. The analysis of the data from the Planck satellite confirmed these findings [15–17], but at the same time confirmed the existence of isotropy anomalies [18].

The full Planck mission data allowed to construct four precise full sky maps that use different cleaning algorithms to remove the influences of the Milky Way [19, 20]. That analysis increases our confidence that the aforementioned isotropy anomalies are not due to instrumental effects, mistakes in the analysis pipeline, or unaccounted foregrounds, which should have been revealed by the wide frequency coverage of Planck. A recent review collects the up-to-date knowledge about these isotropy anomalies [21].

In this article we use the four foreground cleaned full sky maps from the Planck 2015 data analysis to investigate the statistical isotropy of the CMB, especially alignments of multipole vectors within a multipole or with external directions.

The CMB is a relic radiation from the era of photon decoupling, when the first atoms formed and the Universe became transparent. The deviations from a true black-body emission manifest themselves in tiny temperature fluctuations on the celestial sphere of order $\delta T/T_0 \sim 10^{-4} - 10^{-5}$. They depict the energy density inhomogeneities out of which the currently observable large scale structure emerged. There exists a further anisotropy that has the structure of a dipole which is assumed to be mainly due to the relativistic Doppler effect and the aberration induced by the peculiar motion of the Milky Way with respect to the cosmic frame [22]. The current value of this cosmological dipole anisotropy is $(\delta T/T_0)_{\text{dip}} = (3.3645 \pm 0.002) \times 10^{-3}$ [15]. In fact there are still some ambiguities indicating that there

* m.pinkwart@jacobs-university.de

† dschwarz@physik.uni-bielefeld.de

could be other contributions. Analyses of the radio sky with galaxy surveys show an increased radio dipole amplitude [23–26], which could be caused by an intrinsic, non-kinematic CMB dipole.

The peculiar motion induces higher kinematic multipoles as well, but these contributions are very small and therefore usually at most the kinematic quadrupole (DQ) is considered, which has also been removed in the Planck data.

Analyses of the cosmic background radiation are conveniently performed by means of spherical harmonic coefficients and harmonic power spectra, or correlation functions in angular space. When investigating the CMB with respect to possible breaking of statistical isotropy, a third tool has become popular among cosmologists, namely multipole vectors (MPVs) [6, 27, 28]. While spherical harmonic coefficients transform with Wigner’s symbols under a rotation of the celestial sphere, MPVs transform like ordinary three-vectors, i.e. they rotate rigidly with the temperature fluctuations on the sphere which makes them a convenient choice for isotropy analysis.

The structure and outcome of this article is based on the master’s thesis [29]. In Sect. II we review the basic definitions and properties of CMB data analysis by means of the angular power spectrum and we describe our convention of statistical isotropy. Then, in Sect. III we give an overview over three convenient extraction methods for MPVs. In Sect. IV we review the derivation of the probability distribution of MPVs. In Sect. V we shortly describe the Planck data used in the analysis. Sect. VI is dedicated to the introduction of the statistics that we use for the analysis. Sect. VII introduces the four astrophysical directions used in the analysis to estimate sources of multipole anomalies. In Sect. VIII we present the results before discussing them in Sect. IX and giving a short conclusion and outlook in Sect. X.

II. ANGULAR POWER SPECTRUM

The relative fluctuations of CMB temperature, which live on the celestial sphere, are conveniently decomposed according to the irreducible representations of the group of three-dimensional spatial rotations $SO(3)$, namely the orthonormal set of spherical harmonic functions,

$$\frac{\delta T}{T_0}(\mathbf{e}) = \sum_{l=1}^{\infty} \sum_{m=-l}^l a_{lm} Y_{lm}(\mathbf{e}), \quad (1)$$

with the radial unit vector $\mathbf{e} = (\cos(\phi) \sin(\theta), \sin(\phi) \sin(\theta), \cos(\theta))$ pointing towards the direction of observation. The contribution from a given integer number l ,

$$f_l(\mathbf{e}) = \sum_m a_{lm} Y_{lm}(\mathbf{e}), \quad (2)$$

is called a multipole of order l , which describes features at typical angular scales of about $\alpha_l = \pi/l$. The coefficients a_{lm} are called spherical harmonic coefficients. Thanks to the orthonormality of $\{Y_{lm}\}$, i.e., $\int Y_{lm} Y_{l'm'}^* = \delta_{ll'} \delta_{mm'}$, the a_{lm} can be calculated from $\delta T/T_0$ via integration

$$a_{lm} = \int d^3\mathbf{e} \frac{\delta T(\mathbf{e})}{T_0} Y_{lm}^*(\mathbf{e}). \quad (3)$$

Since temperature fluctuations are real, and $Y_{lm}^* = (-1)^m Y_{l,-m}$, the spherical harmonic coefficients obey

$$a_{lm}^* = (-1)^m a_{l,-m}. \quad (4)$$

The particular pattern of the CMB temperature fluctuations cannot be predicted. Instead, temperature fluctuations are modelled as a real, random field on the sphere, or equivalently we model the measured spherical harmonic coefficients as realizations of an ensemble of random variables, subject to condition (4).

A fundamental assumption regarding the temperature fluctuations is *statistical isotropy*, that means

$$\forall R \in SO(3) \forall \mathbf{e}_1, \dots, \mathbf{e}_n \in \mathcal{S}^2 \forall n \in \mathbb{N} : \left\langle \prod_{i=1}^n \frac{\delta T}{T_0}(R\mathbf{e}_i) \right\rangle = \left\langle \prod_{i=1}^n \frac{\delta T}{T_0}(\mathbf{e}_i) \right\rangle, \quad (5)$$

where $\langle \cdot \rangle$ denotes the expectation value of random fields, respectively the ensemble average over all “possible universes”. Correlation functions of temperature fluctuations at different directions should only depend on the angle between them, respectively on the scalar products $\mathbf{e}_i \cdot \mathbf{e}_j$.

Here, we take the point of view of an observer in three-dimensional space that acts with an element of $SO(3)$ on the sky. There exists also the other convention that the three degrees of freedom of three-dimensional rotation are split into a translation on \mathcal{S}^2 – and invariance under such a transformation would then be called homogeneity – and a rotation around a point on \mathcal{S}^2 . The invariance of the latter would then be associated with isotropy. In our work all three symmetry operations are viewed as rotations and thus we only speak about isotropy.

One usually argues that the smallness of the CMB temperature fluctuations provides empirical evidence for statistical isotropy of the Universe and cosmological inflation provides an argument on why the observed patch of the Universe should be isotropic. But there are a priori no other reasons and a detailed study of the observed deviations from isotropy in $\delta T/T_0$ might reveal that statistical isotropy could be violated, for example due to primordial anisotropies.

A trivial consequence of the definition of δT is the vanishing of the one point function, $\langle \delta T(\mathbf{e})/T_0 \rangle = 0$ or $\langle a_{lm} \rangle = 0$. Thus the first non-trivial and most interesting object is the angular two-point correlation or the angular power spectrum C_l , which for an isotropic ensemble is given by $\langle a_{lm}^* a_{l'm'} \rangle = C_l \delta_{ll'} \delta_{mm'}$.

As a result of the initial Gaussianity after inflation and the following linear evolution, this random field is assumed to be Gaussian in the standard theory. That means that higher correlations cannot carry independent information. Thus in the standard model of cosmology all cosmological information is encoded in the angular power spectrum C_l .

Unfortunately, we can only observe one single Universe and therefore the crucial quantity C_l has to be estimated using the data given. The conventional estimator is

$$\hat{C}_l := \frac{1}{2l+1} \sum_{m=-l}^l |a_{lm}|^2, \quad (6)$$

which is unbiased

$$\langle \hat{C}_l \rangle = \frac{1}{2l+1} \sum_m \langle |a_{lm}|^2 \rangle = C_l, \quad (7)$$

but carries a finite variance, called *cosmic variance*

$$\text{var}(\hat{C}_l) = \frac{2}{2l+1} C_l^2. \quad (8)$$

One can obtain a further useful measure by considering the expectation of squared fluctuations

$$\langle (\delta T(\mathbf{e})/T_0)^2 \rangle = \sum_{l=1}^{\infty} \frac{2l+1}{4\pi} C_l, \quad (9)$$

and approximating it by an integral

$$\langle (\delta T(\mathbf{e})/T_0)^2 \rangle \approx \int_{\mathbb{R}} d \log(l) \frac{l(l+1)}{2\pi} C_l =: \int_{\mathbb{R}} d \log(l) \mathcal{D}_l. \quad (10)$$

The quantity \mathcal{D}_l is called the *angular band power spectrum* and determines the contribution of a decimal interval of angular scales to the squared temperature fluctuations. Common plots depicting the temperature anisotropy spectrum usually show this quantity.

III. MULTIPOLE VECTORS

MPVs represent a tool for investigating CMB anisotropies in a very natural manner. They behave like ordinary three-vectors under rotation and they do not distinguish a certain reference frame, unlike the spherical harmonics which incorporate a reference to a chosen z -axis in their definition. In the following, we first introduce MPVs along their first historical appearance in classical electrodynamics and afterwards review different mathematical approaches to the description of functions on the sphere via MPVs. These different approaches do not only show the vast mathematical ingredients, that MPVs allow for, but they are suited to different areas of investigation as well. While the algebraic and tensorial approach yield recursive relations for direct calculation

of the MPVs from a given spherical harmonic decomposition, the coherent state approach gives the MPVs as roots of a complex polynomial. With the help of the latter one can even calculate analytically the joint probability density given a fixed multipole.

A. Origin and Sylvester's theorem

MPVs date back to Maxwell who introduced them in *A treatise on electricity and magnetism*, see [30], in the study of interactions between point sources, respectively monopoles, on his road revealing the classical nature of electrodynamics. A monopole creates an electric potential proportional to $1/r$. Maxwell argued that the potential of two opposite-signed monopoles can be written as a directional derivative of the monopole potential $D_{\mathbf{v}}(1/r)$, where \mathbf{v} denotes the linking vector between the point charges. He continued to the case of $3, 4, \dots$ interacting monopoles and received a potential of the form $D_{\mathbf{v}_1} \dots D_{\mathbf{v}_l}(1/r)$ if l monopoles are involved. Later on it has been noticed that any real, harmonic and homogeneous polynomial on \mathbb{R}^3 can be represented in that form.

Let $f : \mathbb{R}^3 \rightarrow \mathbb{R}$ be a real, harmonic and homogeneous polynomial of degree l in the variables x, y, z . That means $\Delta_{\mathbb{R}^3} f = 0$, implying $\Delta_{\mathcal{S}^2} f = -l(l+1)f$, and $f(\lambda x, \lambda y, \lambda z) = \lambda^l f(x, y, z)$. Any such polynomial defines a polynomial $\tilde{f} = f|_{\mathcal{S}^2} : \mathcal{S}^2 \rightarrow \mathbb{R}$ on the sphere and vice versa. Maxwell's MPV representation states that there exist l unique unit directions $\mathbf{v}_1, \dots, \mathbf{v}_l$, such that f takes on the following form

$$f(x, y, z) = (\mathbf{v}_1 \cdot \nabla) \dots (\mathbf{v}_l \cdot \nabla) \frac{1}{r(x, y, z)} \quad (11)$$

$$\text{with } r(x, y, z) = \sqrt{x^2 + y^2 + z^2}.$$

This statement is also known as *Sylvester's Theorem* which was first proven by James Joseph Sylvester in 1876, see [31].

The expression (11) is equivalent to the in practice more useful expression

$$f(\theta, \phi) = C(\mathbf{e}(\theta, \phi) \cdot \mathbf{v}_1) \dots (\mathbf{e}(\theta, \phi) \cdot \mathbf{v}_l) + r^2 F(\theta, \phi), \quad (12)$$

where θ and ϕ describe the sphere in spherical coordinates and $\mathbf{e}(\theta, \phi) = (x(\theta, \phi), y(\theta, \phi), z(\theta, \phi))/r(x, y, z)$, and F is a homogeneous polynomial in the variables x, y, z of degree $\leq l-2$. Due to the fact that spherical harmonics provide a basis for harmonic functions, each multipole of a spherical harmonic decomposition of CMB fluctuations on the sky can be identified uniquely with a set of MPVs.

B. Extraction of Multipole Vectors

There exist several approaches to MPVs and their calculation from a spherical harmonic decomposition, three

of which we will review briefly in the following. While the approach via coherent states appears to be best suited for the investigation of statistical properties, in this work the tensorial approach has been used to calculate the MPVs numerically [32].

1. Tensorial construction

It have been Copi, Huterer and Starkman who first applied the long forgotten method of MPVs to the analysis of CMB data in [27].

Let $f : \mathbb{R}^3 \rightarrow \mathbb{R}$ be a function. If restricted to the two-sphere it can be decomposed into to spherical harmonics

$$f|_{S^2}(\mathbf{e}) = \sum_{l=0}^{\infty} f_l(\mathbf{e}) := \sum_{l=0}^{\infty} \sum_{m=-l}^l a_{lm} Y_{lm}(\mathbf{e}). \quad (13)$$

The fragments f_l are harmonic and homogeneous polynomials of degree l in x, y, z and as such they are the objects of interest. By definition of homogeneity we have $f_l(\lambda(x, y, z)) = \lambda^l f_l(x, y, z)$ and thus $f_l(x, y, z) = F_{i_1 \dots i_l} e^{i_1} \dots e^{i_l}$, where $e^{i_k} \in \{x, y, z | x^2 + y^2 + z^2 = 1\}$ and $\mathbf{e} = (x, y, z)$ denotes the unit vector in (x, y, z) -direction. In order to guarantee uniqueness of this expression, it is inevitable to impose further restrictions on the coefficients $F_{i_1 \dots i_l}$, which can be regarded as coefficients of a tensor F , and on the product $e^{i_1} \dots e^{i_l}$. Both factors have to be trace-free and symmetric

$$f_l(\mathbf{e}) = F_{i_1 \dots i_l}^{(l)} [e^{i_1} \dots e^{i_l}] =: A^{(l)} \left[v_{i_1}^{(l,1)} \dots v_{i_l}^{(l,l)} \right] [e^{i_1} \dots e^{i_l}]. \quad (14)$$

The brackets denote the symmetric trace-free part of the interior

$$\begin{aligned} [S^{i_1 \dots i_l}] &:= \frac{(l!)^2}{(2l)!} \sum_{k=0}^{\lfloor l/2 \rfloor} (-1)^k \frac{(2l-2k)!}{k!(l-k)!(l-2k)!} \\ &\cdot \delta^{(i_1 i_2 \dots i_{2k-1} i_{2k} S^{i_{2k+1} \dots i_l}) p_1 \dots p_{2k}} \\ &\cdot \delta_{p_1 p_2} \dots \delta_{p_{2k-1} p_{2k}}, \end{aligned} \quad (15)$$

while the parenthesis denote the symmetric part solely

$$S^{(i_1 \dots i_l)} := \frac{1}{l!} \sum_{\sigma \in S_l} S^{i_{\sigma(1)} \dots i_{\sigma(l)}}. \quad (16)$$

Eq. (14) defines the MPVs $\mathbf{v}^{(l,j)}$ and by the use of Eq. (13) they can be calculated uniquely, up to rescaling, from the spherical harmonic data. One recovers F from f_l via integration

$$F_{i_1 \dots i_l}^{(l)} = \frac{(2l+1)(2l)!}{(4\pi)2^l(l!)^2} \int_{S^2} d\mathbf{e} f_l(\mathbf{e}) [e^{i_1} \dots e^{i_l}], \quad (17)$$

and afterwards peels off the first MPV by writing

$$\bar{F}_{i_1 \dots i_l}^{(l)} = \left[v_{i_1}^{(l,1)} a_{i_2 \dots i_l}^{(l,1)} \right], \quad (18)$$

where $a^{(l,1)}$ is a rank $l-1$ tensor. In the same manner one can peel of the second MPV from $a^{(l,1)}$ leaving a rank $l-2$ tensor. Repeating this procedure until a rank 1 tensor is left yields all l MPVs. By performing a more detailed mathematical calculation one can write down a system of equations that relate the a_{lm} and the $\mathbf{v}^{(l,j)}$; for more details see [27]. Copi's MPV calculation program [32], which was used by the authors, evaluates this system and returns the MPVs.

Finally note that no information is lost in the transition from spherical harmonics to MPVs. For each l there are $2l+1$ real degrees of freedom in the spherical harmonic decomposition, namely the real and imaginary parts of all a_{lm} with $m \geq 0$. The reason is that the realness of f_l imposes the constraints $a_{lm}^* = (-1)^m a_{lm}$, implying that all coefficients for $m < 0$ can be expressed by the coefficient with $m' = -m > 0$, while the coefficient for $m = 0$ is real, see Eq. (4). This yields the $2l+1$ real degrees of freedom. On the other hand, l unit vectors and an amplitude constitute as well $2l+1$ real degrees of freedom since due to the normalization condition a single unit vector in \mathbb{R}^3 has 2 degrees of freedom, and the amplitude is just a scalar which contributes one further degree of freedom.

2. Algebraic construction

Katz and Weeks [28] applied Bézout's theorem from algebraic geometry to proof Sylvester's theorem. The advantage of this approach is its mathematical sophisticated nature. Furthermore, like the tensorial approach, it yields an iterative prescription calculating the MPVs, and even an explicit expression for the residual polynomial F can be obtained. This approach has a long history dating back to Hilbert and Courant, see [33].

A homogeneous polynomial P of degree l on \mathbb{R}^3 may be written uniquely up to reordering and rescaling as

$$\begin{aligned} P(x, y, z) &= \lambda(a_1 x + b_1 y + c_1 z) \dots \\ &\dots (a_l x + b_l y + c_l z) \\ &+ (x^2 + y^2 + z^2) R, \end{aligned} \quad (19)$$

where R denotes a residual polynomial which is homogeneous of degree $l-2$. If $l < 2$ one sets $R \equiv 0$, and for $l = 2$ the zero can be replaced by a non-vanishing constant.

Let now f be an arbitrary, especially not necessarily homogeneous, polynomial of degree l restricted to the two-sphere. It can be written as a sum of homogeneous polynomials of degree i , f_i , via $f = \sum_{i=0}^l f_i$. According to (19), up to reordering and rescaling f_i can be decomposed into linear factors and a residual polynomial $f_i = \lambda_i \prod_{j=1}^i (v_x^{(l,j)} x + v_y^{(l,j)} y + v_z^{(l,j)} z) + R_{i-2}(x, y, z)$. Since R_{i-2} is homogeneous of degree $i-2$, the sum $f'_{i-2} := f_{i-2} + R_{i-2}$ is again homogeneous of degree $i-2$. Applying (19) recursively on the rest of the sum eventu-

ally results in

$$f(x, y, z) = \sum_{i=0}^l \lambda_i \prod_{j=1}^i (v_x^{(i,j)} x + v_y^{(i,j)} y + v_z^{(i,j)} z) \quad \text{on } \mathcal{S}^2. \quad (20)$$

The scalar product of MPVs with the unit vector in (θ, ϕ) -direction is given by the $i = l$ -term while the rest of the sum constitutes the residual polynomial F . For more details we refer to [28].

3. Construction via Bloch coherent states

Dennis used a very physical approach to proof Sylvester's theorem and associate MPVs to spherical harmonics [34]. A complex spin-state in non-relativistic one-particle quantum mechanics with spin 1/2 can be represented via one point on the two-sphere. This concept is known as the *Bloch Sphere*. Extending this concept to higher integer spins and assuming the state is real yields Sylvester's theorem. The big advantage of this approach is the capability of calculating a joint probability density for the MPVs using techniques from random polynomial theory. An analytic result for the joint probability density in principal allows to compute confidence levels for certain CMB statistics analytically.

A similar approach, but with slightly different focus, was used in [6]. By rotating the highest weight spin state one receives *Bloch coherent states*, i.e. those coherent states associated to $SO(3)$, and the overlap of such a coherent state at rotation angles θ and ϕ with a normalized spin state gives, after stereographic projection, the Majorana polynomial below. Using the Bloch states one can define an extended version of the von Neumann entropy, called Wehrl entropy, which measures quantum randomness.

The formalism below has already been used by Schupp in 1999 in the proof of some special cases of Lieb's conjecture for the Wehrl entropy of Bloch coherent states, see [35].

Let $|\Psi\rangle$ denote a quantum mechanical state with definite integer spin l , i.e., an eigenstate of the total angular momentum operator \hat{L}^2 . It corresponds to a harmonic function in the language of the previous subsections. The eigenstate property allows to expand the state in terms of eigenstates of the z -component of the angular momentum operator \hat{L}_z

$$|\Psi\rangle = \sum_{m=-l}^l \Psi_m |m, l\rangle, \quad \Psi_m \in \mathbb{C}, \quad (21)$$

which in position space is nothing else than the spherical harmonic decomposition. Let $\hat{R}_z(\phi)$ denote the operator which executes a rotation by the angle ϕ around the z -axis and $\hat{R}_y(\theta)$ the rotation by θ around the y -axis and define

$$|m, l; \theta, \phi\rangle := \hat{R}_z(\phi) \hat{R}_y(\theta) |m, l\rangle. \quad (22)$$

This is an eigenstate of the $\mathbf{e}(\theta, \phi)$ -parallel component of \hat{L} . The spherical harmonics are then given by

$$Y_{lm}(\theta, \phi) = \sqrt{\frac{2l+1}{4\pi}} \langle 0, l; \theta, \phi | m, l \rangle. \quad (23)$$

The state $|\Psi\rangle$ can now be expressed via spherical harmonics by projecting on the rotated $m = 0$ state

$$\Psi(\theta, \phi) := \langle 0, l; \theta, \phi | \Psi \rangle = \sqrt{\frac{4\pi}{2l+1}} \sum_{m=-l}^l \Psi_m Y_{lm}(\theta, \phi). \quad (24)$$

After stereographic projection from the south pole

$$\zeta(\theta, \phi) = \tan(\theta/2) \exp(i\phi), \quad (25)$$

and using some group theory, the spin spate $|\Psi\rangle$ can be decomposed according to the $SL(2, \mathbb{C})$ basis functions $\mu_{k-l} \zeta^k$ with $k \in \mathbb{N}_0$

$$f_\Psi(\zeta) := \langle -l, l; \zeta | \Psi \rangle = \frac{\exp(-il \arg(\zeta))}{(1 + |\zeta|^2)^l} \sum_{m=-l}^l \Psi_m \mu_m \zeta^{l+m}, \quad (26)$$

with the numerical factor $\mu_m = (-1)^{l+m} \sqrt{\binom{2l}{l+m}}$. The representation (26) of the state is called *Majorana function*. It is a product of a ζ -dependent factor and a polynomial of degree $2l$ in ζ which contains all the information about the original state. This polynomial is called *Majorana polynomial* and it determines the roots of the Majorana function. Since it is a polynomial of degree $2l$ in the complex variable ζ , it possesses $2l$ complex roots according to the fundamental theorem of algebra, and therefore it can be factorized

$$f_\Psi(\zeta) = \frac{\exp(-il \arg(\zeta))}{(1 + |\zeta|^2)^l} (-1)^{2l} \Psi_{m=l} \prod_{n=1}^{2l} (\zeta - \zeta_n). \quad (27)$$

The $2l$ roots can be back-projected onto the Riemannian sphere $\mathcal{S}^2 \cong \hat{\mathbb{C}} \cong \mathbb{C} \cup \{\infty\}$. These back-projected roots $\mathbf{v}(\zeta_n)$ are called *Majorana vectors*. In the case of a real $\Psi(\theta, \phi)$ they are identical to the MPVs

$$\mathbf{v}^{(l,j)} \equiv \mathbf{v}(\zeta_j) \quad (28)$$

for a given l .

The Majorana function of the rotated state obeys $f_{\hat{R}_{v,\phi}\Psi}(\zeta) = f_\Psi(MT(\zeta))$, where MT denotes a unitary Möbius transformation. Consequently its zeros also transform under a unitary Möbius transformation. After back projection this transformation corresponds to a rotation through $SO(3)$. Majorana vectors rotate rigidly like ordinary three-vectors.

A further property of Majorana vectors is their appearance in antipodal pairs if the original state is real

$$f_\Psi(-1/\zeta^*) = f_\Psi(\zeta)^*. \quad (29)$$

Hence, ζ is a root of the Majorana function if and only if $-1/\zeta^*$ is a root, but $-1/\zeta^*$ is the image under the stereographic projection of the antipode of the Majorana vector determined by ζ . This property does not hold if the original state is complex. Complex functions on the sphere cannot be represented by l MPVs.

There have been several further approaches to MPVs, for example by investigating their topological implications in [36].

IV. STATISTICAL PROPERTIES OF MULTIPOLE VECTORS

The spherical harmonic coefficients a_{lm} of the CMB temperature fluctuations are attached with a notion of randomness implied by inflationary fluctuations. Standard inflationary scenarios lead to Gaussianity of these coefficients. Whether they are really Gaussian or not, they definitely constitute a set of random variables. The MPVs, which depend only on these coefficients, inherit the randomness from these coefficients. One may now ask what kind of probability distribution they obey exactly.

Dennis and Land attended to this question first in [37], followed up by [38]. For this purpose the coherent state approach turns out to be especially useful because MPVs are the roots of a complex polynomial whose coefficients are the a_{lm} times some numerical factor. Therefore we have to deal with the probability density of roots of random polynomials which is a currently much studied field of statistical mathematics.

In App. B we present some first ideas on how to apply results from random matrix theory and the theory of Gaussian analytic functions on the problem of the joint probability distribution of MPVs.

This section is intended to provide a review of the derivation of the MPV joint probability distribution. The essential properties are the statistical decoupling of MPVs at different angular scales and the non-trivial correlation between MPVs at a given angular scale π/l . Furthermore, it is important to note that even if the underlying temperature fluctuation field is Gaussian, the MPV distribution is not and hence it is not enough to consider only one- and two-point functions, but one needs the full set of all n -point functions, where $n = 1, \dots, l$ for a given l . Although an explicit expression for the probability distribution of the MPVs has been found before in [37], it turns out to be of limited use for practical purposes, except for the lowest multipoles $l = 1, 2, 3$. In this work we use Monte Carlo methods, which appear to yield results faster than numerical integration of the analytic expression.

A. Isotropy and Gaussianity

Let us first focus on the description of isotropy and Gaussianity in the CMB data and the difference between

both.

The temperature fluctuation field is Gaussian if for all $n \in \mathbb{N}$ and all $\mathbf{e}_i \in \mathcal{S}^2$ with $i = 1, \dots, n$ the probability distribution of $\delta T/T_0$ follows

$$p(\delta T/T_0) = \frac{1}{\mathcal{N}} \exp \left(-\frac{1}{2} \sum_{ij} \left(\frac{\delta T}{T_0} \right)_i (D^{-1})_{ij} \left(\frac{\delta T}{T_0} \right)_j \right), \quad (30)$$

with $(\delta T/T_0)_i = \delta T(\mathbf{e}_i)/T_0$ and some normalization constant \mathcal{N} . The matrix D is the correlation matrix $D_{ij} = \langle (\delta T/T_0)_i (\delta T/T_0)_j \rangle$. The Gaussianity of δT stems from the Gaussianity of the a_{lm} that obey

$$p(\{a_{lm}\}) = \frac{1}{\mathcal{N}'} \exp \left(-\frac{1}{2} \sum_{l,l',m,m'} a_{lm}^* (C^{-1})_{lm'l'm'} a_{l'm'} \right), \quad (31)$$

with $C_{lm'l'm'} = \langle a_{lm}^* a_{l'm'} \rangle$ and \mathcal{N}' some normalization constant which is in general different from \mathcal{N} . A Gaussian field is fully characterized by its correlation matrix and if we demand isotropy additionally, then $C_{lm'l'm'} = \delta_{mm'} \delta_{ll'} C_l$. In this case we have

$$p(\{a_{lm}\}) = \prod_{lm} \frac{\exp(-|a_{lm}|^2/(2C_l))}{\sqrt{2\pi C_l}}, \quad (32)$$

i.e., the a_{lm} are identically and independently distributed complex Gaussian random variables with variance C_l , or alternatively all real and imaginary parts $\Re a_{lm}$, $\Im a_{lm}$ as well as a_{l0} are identically and independently distributed real Gaussian random variables with variance C_l .

Isotropy and Gaussianity do not necessarily imply each other. Consider for example a distribution which is gained by an isotropic and Gaussian distribution via introducing a cutoff for large values of $|a_{lm}|$. By this we mean $p(a_{lm}) = 0$ if $|a_{lm}| > \kappa \in \mathbb{R}$ for all l and m . This distribution is not fully Gaussian any longer but does not lose its isotropy. On the other hand a general Gaussian distribution does not need to be isotropic.

B. Probability distribution

It turns out that the joint probability density for the MPVs of fixed angular momentum l is the same for all so called *completely random* sets of a_{lm} , this means that the probability density of the coefficients, $p(a_{lm})$, depends only on the sum $\sum_m |a_{lm}|^2$, respectively on the power spectrum estimator \hat{C}_l , see [37] and [38]. An isotropic and Gaussian distribution is of course included in the set of completely random distributions, see Fig. 1. Note that complete randomness does not require the a_{lm} to be statistically independent. Rather, if they are statistically independent and completely random, they automatically have to be Gaussian. Gaussianity itself in combination with complete randomness implies statistical isotropy, but not vice versa, and therefore we shall insist on complete randomness for the rest of this publication and treat

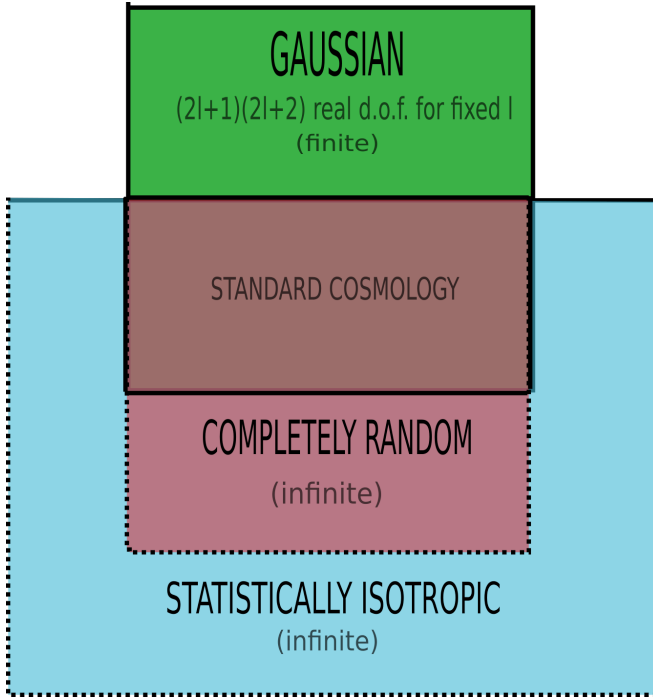


FIG. 1: Visualization of the relation between Gaussianity, statistical isotropy and complete randomness. Dotted lines denote probable infinite extension.

it as a basic assumption which incorporates statistical isotropy if Gaussianity is given. The most important class of distributions for cosmology is given by the intersection of completely random and Gaussian a_{lm} , which we call “standard cosmology” in Fig. 1. Since no sizable deviations from Gaussianity have been observed so far, see e.g. [13] or [17], assuming that Gaussianity holds true allows for investigating isotropy solely.

For fixed l the set of Gaussian distributions is described by a finite number of degrees of freedom, since due to Wick’s theorem the expectation values $\langle a_{lm} \rangle$ and the two-point functions $\langle a_{lm} a_{l'm'}^* \rangle$ uniquely determine the distribution. Respecting the reality condition $a_{lm}^* = (-1)^m a_{l,-m}$ yields $2l+1+(2l+1)^2 = (2l+1)(2l+2)$ real degrees of freedom. The sets of statistically isotropic as well as completely random distributions are a priori not bounded in their degrees of freedom. Any n -point function, with $n \in \mathbb{N}$, contributes to the knowledge of the distribution. Hence both distributions have at least a countably infinite set of degrees of freedom. The intersection of the completely random case and the Gaussian case coincides with the intersection of the isotropic and Gaussian case. Nevertheless, there exist completely random a_{lm} which are not Gaussian, as for for example a delta distribution $\delta(\hat{C}_l)$. In principle there can also exist statistically isotropic, non-Gaussian distributions which are not completely random by just building some quantity \mathcal{Q} out of the a_{lm} that is rotationally invariant but no function of \hat{C}_l and considering the distribution $p(\mathcal{Q})$.

That completely random distributions form a subset of statistically isotropic ones can be seen as follows: Since a rotation \hat{R} acts on \mathbb{C}^{2l+1} as a special unitary transformation, its determinant vanishes and therefore

$$\langle \prod_i \mathcal{O}_i(\hat{R}(\mathbf{e}_i)) \rangle = \int \prod_m da_{lm} \prod_i \mathcal{O}_i(\{a_{lm}\}) p(\{\hat{R}^{-1} a_{lm}\}). \quad (33)$$

The property of statistical isotropy reduces to the rotational invariance of the joint probability. In the completely random case we have $p(\{a_{lm}\}) = p(\sum_m |a_{lm}|^2)$. Let the unitary operator corresponding to \hat{R}^{-1} acting on \mathbb{C}^{2l+1} be denoted by \mathcal{D} (which is related to Wigner’s D-matrix, see [39]) and write the set of a_{lm} for fixed l as a vector $\mathbf{a}_l \in \mathbb{C}^{2l+1}$, then

$$\begin{aligned} \hat{R} \left(\sum_m |a_{lm}|^2 \right) &= \sum_m |\hat{R}(a_{lm})|^2 = (\mathcal{D}\mathbf{a}_l)^\dagger \cdot (\mathcal{D}\mathbf{a}_l) \\ &= \mathbf{a}_l^\dagger \mathcal{D}^\dagger \mathcal{D} \mathbf{a}_l = \mathbf{a}_l^\dagger \cdot \mathbf{a}_l \\ &= \sum_m |a_{lm}|^2, \end{aligned} \quad (34)$$

due to the unitary representation of $SO(3)$ as $SU(2)$. Hence, completely random sets of a_{lm} always obey statistical isotropy.

For CMB analysis one needs the joint probability distribution of MPVs because inside one multipole they are not independent of each other. This stems directly from the behavior of random roots which tend to repel each other. Contrary to this, the MPVs from different multipoles are perfectly independent.

The first calculation of the joint probability densities of random spin- l states was performed in 1995 by Hannay, see [40]. He notes that the Majorana function equals exactly the Bargmann function of the spin state in the Segal-Bargmann space [41]. This representation of quantum states can be seen as a third leg of standard quantum mechanics accompanying Heisenberg’s matrix- and Schrödinger’s wave function quantum mechanics.

It turns out that in the completely random case the n -point density can be written as a normalized permanent

$$\begin{aligned} p_n^l(\zeta_1, \dots, \zeta_n, \zeta_{l+1} = -1/\zeta_1^*, \dots, \zeta_{l+n} = -1/\zeta_n^*) \\ = \frac{1}{\pi^n} \frac{\text{per}(C - B^\dagger A^{-1} B)}{\det(A)}, \end{aligned} \quad (35)$$

with

$$\begin{aligned}
f_i &:= f_\Psi(\zeta_i) \quad \text{Majorana function evaluated at the root} \\
A_{ij} &= \langle f_i f_j^* \rangle \\
&\stackrel{\text{isotropy}}{=} \sum_{m,m'=-l}^l (-1)^{m+m'} \left[\binom{2l}{l+m} \binom{2l}{l+m'} \right]^{1/2} \\
&\quad \cdot \underbrace{\langle a_{lm} a_{l m'}^* \rangle}_{=C_l \delta_{mm'}} \zeta_i^{l+m} (\zeta_j^*)^{l+m'} \\
&= C_l \sum_{m=-l}^l \binom{2l}{l+m} (\zeta_i \zeta_j^*)^{l+m} = C_l \sum_{r=0}^{2l} \binom{2l}{r} (\zeta_i \zeta_j^*)^r \\
&= C_l (1 + \zeta_i \zeta_j^*)^{2l} \tag{36}
\end{aligned}$$

$$B_{ij} = \langle f_i f_j'^* \rangle \stackrel{\text{isotropy}}{=} C_l 2l \zeta_i (1 + \zeta_i \zeta_j^*)^{2l-1} \tag{37}$$

$$C_{ij} = \langle f_i' f_j'^* \rangle \stackrel{\text{isotropy}}{=} C_l 2l (1 + 2l \zeta_i \zeta_j^*) (1 + \zeta_i \zeta_j^*)^{2l-2}, \tag{38}$$

where the second equalities only hold in the isotropic case, see also [38]. The matrices A, B, C are $(2n \times 2n)$ -matrices. Calculating A^{-1} and inserting the explicit formulas from (36)-(38) yields the joint probability density of $1 \leq n \leq l$ MPVs. Note that here the function f can in principle be complex! Isotropy and Gaussianity enter the game when the precise expressions (36)-(38) are inserted. Even though the function f can be complex, one should remember that the representation of the function by MPVs is possible only for real functions!

An alternative derivation of the full joint density ($n = l$), made by Dennis in [38], uses the fact that the coefficients of any polynomial can be expressed by a symmetric polynomial of its roots leading to the full joint density

$$\begin{aligned}
p_l^l(\{\zeta_i\}) &= \frac{(2l-1)!! \prod_{j=1}^{2l} j!}{(2\pi)^l l! \prod_{j=1}^l |\zeta_j|^2} \\
&\quad \cdot \frac{\prod_{j,k=1, j < k}^{2l} |\zeta_j - \zeta_k|}{\left(\sum_{\sigma \in S_{2l}} \prod_{j=1}^{2l} (1 + \zeta_j \zeta_{\sigma(j)}^*) \right)^{l+1/2}}. \tag{39}
\end{aligned}$$

When projecting back to the sphere, the Jacobi determinant for this transformation has further to be taken into account. Note that f has to be real for Eq. (39) to be valid, since the result was obtained by implicitly setting $\zeta_{l+i} = -1/\zeta_i^*$ which is only true for real Majorana polynomials.

In the case $n = 1$ the distribution of MPVs on one hemisphere of the two-sphere simplifies to a uniform distribution

$$p_1^l([\mathbf{v}]) = p(\theta, \phi) = \frac{1}{2\pi} \tag{40}$$

according to the surface measure. So when drawing MPVs from an ensemble of a_{lm} , the first MPV one draws is always uniformly distributed. For a derivation of (40) see App. A.

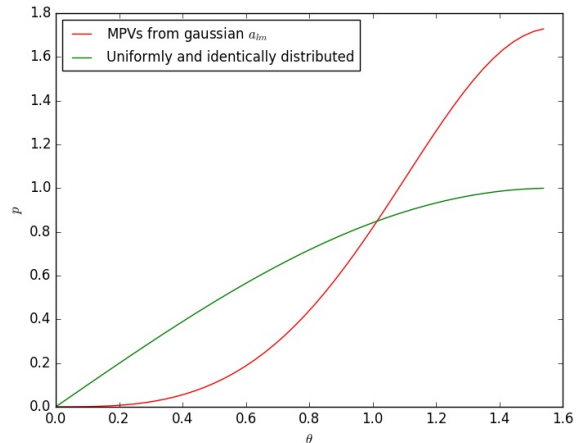


FIG. 2: Comparison of two-point density of MPVs drawn from a Gaussian ensemble of a_{lm} and identically uniformly distributed pseudo-MPVs for $l = 2$

Since MPVs rotate rigidly their density depends only on the relative angle. Thus, for $l = n = 2$ one of the two vectors can be fixed to an arbitrary direction, without loss of generality to the north pole, and the second one encloses an angle Θ with the first one. The two-point density is then given by [38]

$$p_2^2(\Theta) = \frac{27 \sin^3(\Theta)}{(3 + \cos^2(\Theta))^{5/2}}. \tag{41}$$

For comparison imagine a world in which the MPVs are uniformly and independently distributed on the upper hemisphere. Then the first MPV can again be fixed to the north pole and the second is still uniformly distributed on the upper hemisphere. In this case the two-point density would be $p_{\text{uni}}(\Theta) = \sin(\Theta)/2$. Both probability densities are normalized in a way such that $\int_0^{\pi/2} d\Theta p(\Theta) = 1$. In Fig. 2 the two densities are plotted together. One can see that the interaction of MPVs leads to repulsion. Bigger angles are more probable in the case of real MPVs than in the case of uniformity and independence. Such a behavior is characteristic for roots of random polynomials.

The results from (35) are a priori complicated expressions, even for the case $n = 3$, whose integration does not allow for a faster numerical computation of confidence levels than a full Monte Carlo simulation.

V. CMB DATA AND SIMULATION

For our analysis we make use of the Planck 2015 full-sky CMB intensity maps, see [42], with $N_{\text{side}} = 2048$ and treat it within HEALPy, which is a HEALPix [43] implementation for python, see [44].

The Planck full-sky maps are provided in nine different frequency bands. These maps have been foreground

l	COMMANDER	NILC	SEVEM	SMICA
2	(6.9, 21.2) (119.1, 18.2)	(12.8, 20.3) (117.5, 20.1)	(13.3, 26.2) (83.6, 12.3)	(5.7, 23.7) (121.5, 21.9)
3	(25.6, 8.8) (86.3, 38.4) (317.7, 5.0)	(23.2, 9.3) (86.8, 37.7) (315.3, 7.9)	(33.0, 5.4) (61.3, 35.0) (140.5, 0.6)	(22.1, 8.8) (88.1, 38.8) (314.8, 10.5)
4	(69.5, 3.2) (207.5, 72.6) (211.2, 36.7) (333.4, 29.1)	(69.9, 4.5) (203.9, 70.5) (212.6, 40.0) (333.5, 27.7)	(71.1, 19.2) (189.4, 73.0) (201.7, 38.0) (336.5, 27.3)	(68.8, 2.2) (207.8, 38.5) (214.8, 69.9) (335.9, 26.1)
5	(43.3, 33.3) (98.7, 35.7) (174.0, 3.9) (232.1, 54.2) (287.4, 31.6)	(44.2, 35.8) (96.8, 36.1) (175.2, 3.4) (232.4, 55.3) (286.1, 31.6)	(51.5, 28.2) (79.8, 35.3) (174.2, 3.8) (232.1, 58.2) (290.1, 18.9)	(44.3, 36.7) (98.3, 36.2) (175.7, 3.3) (234.9, 55.3) (285.2, 32.8)

TABLE I: MPVs from $l = 2$ to $l = 5$ in galactic coordinates (l, b) in deg with precision of one decimal.

All MPVs have been taken to lie in the northern hemisphere and for a given multipole they were ordered according to their value of the galactic longitude. MPVs in the same line cannot necessarily be identified with each other since they are not a priori ordered inside of a given multipole.

cleaned to produce best estimates of intensity and polarization of the measured CMB signal from the sky after instrumental and known systematical effects, like the dipole and quadrupole (DQ) induced by the motion of Sun and Earth with respect to the cosmic frame, the light from the zodiac cloud, and most important galactic foregrounds (synchrotron radiation, free-free emission, thermal dust, CO lines, anomalous microwave radiation) have been removed. Using four different cleaning algorithms, foreground cleaned full-sky maps of CMB temperature intensity are constructed; for the details of the component separation process we refer to [19]. These different cleaning algorithms, are called COMMANDER, NILC, SEVEM and SMICA. Polarization maps are also created by these algorithms but there are still systematic effects at large angular scales that could not be removed and fully identified wherefore all multipoles $l < 20$ are erased from them – in our work we have used only the intensity maps. All four cleaned full-sky maps have an angular resolution of about $5'$ and are provided in fits-format usable with HEALPix with $N_{\text{side}} = 2048$ in nested ordering and galactic coordinates.

The four maps have been used to extract the MPVs up to $l = 50$ by using a tensorial algorithm [32], see also Sect. III B 1. A list of the MPVs for the multipoles $l = 2, 3, 4, 5$ can be found in Tab. I, text files containing the MPVs for higher l are provided at <https://github.com/MPinkwart/MPV-files-Pinkwart-Schwarz>.

VI. STATISTICS USED FOR ANALYSIS

One needs statistics that deliver information about both intra-multipole alignments and alignments of multipoles with some given astrophysical direction, which in the following will be referred to as outer direction. Furthermore, possible statistics are not allowed to depend on the ordering of MPVs for a fixed l since this ordering is completely arbitrary and contains no information. Additionally, the statistics may not depend on the hemisphere, since MPVs are rather lines than vectors. Eventually, they may not be sensitive to the equator since the gluing mechanism at the equator should be hidden. In the following, intra-multipole statistics are sometimes also referred to as *inner statistics* and statistics that investigate correlations with outer directions as *outer statistics*.

We used the following two outer statistics

$$S_{\mathbf{D}}^{\parallel}(l) := \frac{1}{l} \sum_{i=1}^l |\mathbf{v}^{(l,i)} \cdot \mathbf{D}| \quad (42)$$

$$S_{\mathbf{D}}^v(l) := \frac{2}{l(l-1)} \sum_{1 \leq i < j \leq l} |(\mathbf{v}^{(l,i)} \times \mathbf{v}^{(l,j)}) \cdot \mathbf{D}|, \quad (43)$$

where $\mathbf{v}^{(l,i)}$ denotes the i^{th} MPV belonging to multipole l and \mathbf{D} some outer direction, which will be specified in Sect. V.

Furthermore, we use two inner statistics

$$S^{\parallel}(l) := \frac{2}{l(l-1)} \sum_{1 \leq i < j \leq l} |\mathbf{v}^{(l,i)} \cdot \mathbf{v}^{(l,j)}| \quad (44)$$

$$S^v(l) := \frac{6}{l(l-1)(l-2)} \sum_{1 \leq i < j < k \leq l} |(\mathbf{v}^{(l,i)} \times \mathbf{v}^{(l,j)}) \cdot \mathbf{v}^{(l,k)}|. \quad (45)$$

All statistics are normalized such that they take values in the unit interval $[0, 1]$. Each summand in every statistic ranges from 0 to 1 while the number of summands is $l = \binom{l}{1}$ for $S_{\mathbf{D}}^{\parallel}$, $l(l-1)/2 = \binom{l}{2}$ for S^{\parallel} and $S_{\mathbf{D}}^v$, and $l(l-1)(l-2)/6 = \binom{l}{3}$ for S^v .

Statistic $S_{\mathbf{D}}^{\parallel}$ measures the alignment of a multipole with an outer direction while $S_{\mathbf{D}}^v$ measures the orthogonality of a multipole with respect to this outer direction. Statistic S^{\parallel} measures a possible linearity of the respective multipole itself while S^v measures possible planarity.

Let $X^{l,i} := |\mathbf{v}^{(l,i)} \cdot \mathbf{D}|$, then the expectation value of $S_{\mathbf{D}}^{\parallel}$ is

$$\langle S_{\mathbf{D}}^{\parallel}(l) \rangle = \frac{1}{l} \sum_{i=1}^l \langle X^{l,i} \rangle = \frac{1}{2}. \quad (46)$$

This result holds for all types of completely random a_{lm} . Due to the correlation of MPVs inside one multipole the

variance of $S_{\mathbf{D}}^{\parallel}$ is

$$\text{Var}(S_{\mathbf{D}}^{\parallel}(l)) = \frac{1}{l^2} \left(\frac{l}{12} - \frac{l(l-1)}{4} + 2 \sum_{1 \leq i < j \leq l} \langle X^{l,i} X^{l,j} \rangle \right), \quad (47)$$

where for the calculation of $\langle X^{l,i} X^{l,j} \rangle$ one uses the two-point density (41), yielding

$$\text{Var}(S_{\mathbf{D}}^{\parallel}(2)) = \frac{1}{4} \left(-\frac{1}{3} + \frac{2}{3} \left(6 - \frac{10}{\sqrt{3}} \right) \pi \right) \approx 0.035. \quad (48)$$

If the MPVs would not be correlated but all independent, $S_{\mathbf{D}}^{\parallel}$ would follow a slightly modified Irwin-Hall distribution, see [45, 46],

$$p_{S_{\mathbf{D}}^{\parallel}(l)}(s) = \frac{l}{2(l-1)!} \sum_{k=0}^l (-1)^k \binom{l}{k} (ls-k)^{l-1} \text{sgn}(ls-k), \quad (49)$$

which would result in a variance of $S_{\mathbf{D}}^{\parallel}(2)$ of about 0.042 which is slightly larger than the variance in the completely random case, showing again that the intra-multipole correlation tightens confidence regions. Note that in our analysis we do not use analytical results, since the numerical computation of confidence levels using the full joint probability (39) turns out to be numerically more demanding than a simple Monte Carlo simulation.

In order to compare the analytical results with the numerics, we consider 1000 maps from isotropic and Gaussian random a_{lm} and compare their MPV statistics with the one from the cleaned Planck maps. From Fig. 7a one deduces that the theoretical result (48) for the variance is compatible with the numerical result for the 1σ -region because $\sqrt{0.035} \approx 0.187$.

To characterize and quantify a possible violation of the completely random hypothesis, we introduce a notion of likelihood suggested in [47]. Let us first define what we mean by *p-value*: Let $S_{i,l}$ be the data point of statistic $S_i(l)$ received by one of the four Planck maps, where $i \in \{1, 2, 3, 4\}$ runs through the four statistics. Define the p-value of this data point as

$$P(S_{i,l}) := \int_0^{S_{i,l}} ds p_{S_i(l)}(s), \quad (50)$$

i.e. small ($\ll 1$) as well as large (≈ 1) p-values indicate unusual behavior. Let now $S_{i,l}^M$ denote a data point as above received from map M (COMMANDER, NILC, SEVEM or SMICA). We define the *outer likelihood*

$$L_{l,\mathbf{D}}^{\text{outer}}(M) := 4^2 \prod_{\text{outer}} P(S_{i,l}^M) (1 - P(S_{i,l}^M)), \quad (51)$$

as well as the *inner likelihood*

$$L_l^{\text{inner}}(M) := 4^2 \prod_{\text{inner}} P(S_{i,l}^M) (1 - P(S_{i,l}^M)), \quad (52)$$

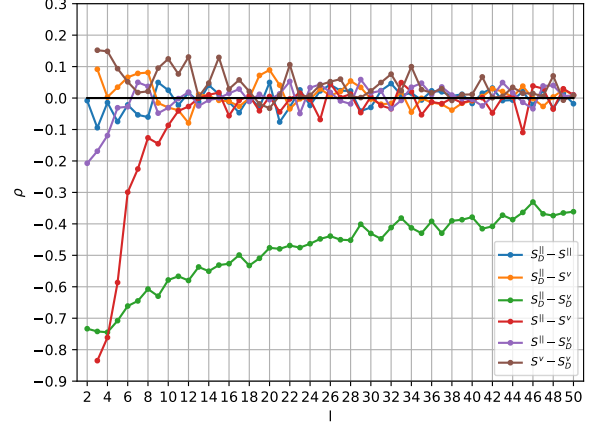


FIG. 3: Linear correlation coefficients of statistics based on a Monte Carlo simulation with 1000 ensembles of a_{lm} . The combination $S^v - S_{\mathbf{D}}^v$ is the one mainly used in previous studies by means of correlations between area vectors. It shows only slight correlation at the largest angular scales.

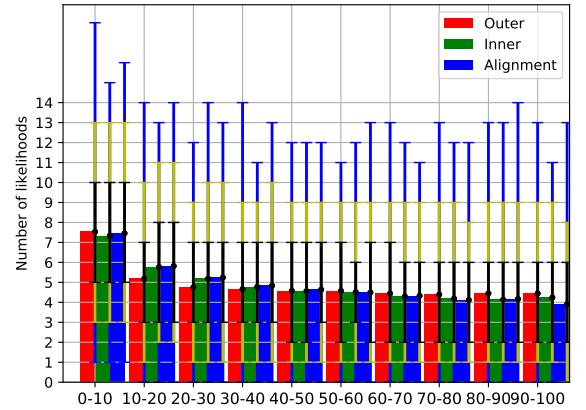


FIG. 4: Histograms for all three likelihoods calculated with thousand ensembles of Monte Carlo a_{lm} in the range $2 \leq l \leq 50$. The thin bars signify 1σ (black), 2σ (yellow) and 3σ (blue).

and the *alignment likelihood*

$$L_{l,\mathbf{D}}^{\parallel}(M) := 4^2 \prod_{\parallel} P(S_{i,l}^M) (1 - P(S_{i,l}^M)). \quad (53)$$

The inner likelihood measures anomalies inside a given multipole, while the outer likelihood measures the anomalies with respect to some outer direction. Eventually, the alignment likelihood measures the combined effect of alignment with an outer direction and intra-multipole alignment.

Before studying the Planck maps we need to under-

stand the correlation between statistics. For low l Fig. 3, as well as Figs. 19a and 19b in App. C, show that the outer as well as the inner statistics are highly (anti-)correlated. For higher l the linear correlation of inner statistics vanishes, see Fig. 20a in App. C, the outer statistics keep their correlation on a wide range of scales, see Fig. 20b in App. C. Apart from statistical fluctuations the alignment statistics show nearly no correlation at all. Naively one would expect the inner and outer correlations to effect the behavior of the likelihoods, but Fig. 4 shows that the distribution of likelihoods in the range $2 \leq l \leq 50$ is nearly the same for all three considered types of likelihoods. The definition of the likelihoods itself favors smaller values of the likelihoods, but inner and outer correlations show no sizable effect if compared to the uncorrelated alignment statistics.

If we use likelihoods that incorporate only one single statistic, and not the combination of two statistics, the appearance of the histograms change, see Fig. 21 in App. C, but the conclusion we can draw from its analysis turns out to be in fact the same as for the combined likelihoods.

VII. TEST DIRECTIONS

We use the following four physical directions, whose possible influences should have different and independent physical reasons:

- The Cosmic Dipole $(l, b) = (264.00^\circ, 48.24^\circ)$, taken from [15]. A correlation with this direction could imply that the nature of the kinematic dipole is not fully understood yet, that it has not been removed from the data properly, that the CMB contains an intrinsic dipole for itself, or that the calibration pipeline is odd.
- The Galactic Pole $(l, b) = (0^\circ, 90^\circ)$. Galactic foregrounds which are aligned with the disk of the Milky Way could give rise to an alignment with the Galactic Pole.
- The Galactic Center $(l, b) = (0^\circ, 0^\circ)$. The foreground pollution due to the inner part of the Milky Way could still be present in the cleaned maps. A correlation with this direction would indicate that these residuals still play an important role in data analysis.
- The Ecliptic Pole $(l, b) = (96.38^\circ, 29.81^\circ)$ (Transformed from ecliptic to galactic coordinates with the NASA conversion tool [48].) The lowest multipoles are known to correlate unusually with the Ecliptic. Foreground pollution from the Solar System could cause such a correlation.

In Fig. 5 we plot the MPVs for all pipelines at $l = 2$ together with the four outer directions and the intersection

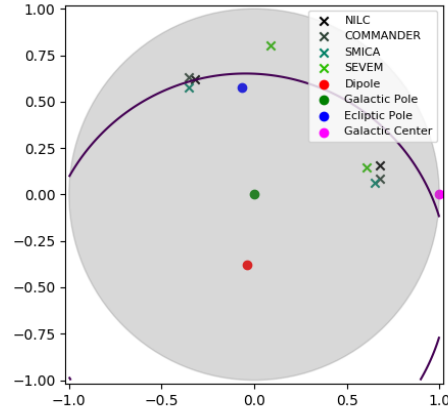


FIG. 5: MPVs for $l = 2$ and physical directions in stereographic projection. The violet curve shows the plane orthogonal to the Cosmic Dipole.

of the plane orthogonal to the Cosmic Dipole with the celestial sphere in stereographic projection from the south pole. One should note that the stereographic projection does not preserve distances. Arcs close to the south pole get stretched with respect to arcs close to the north pole. But since we only consider one hemisphere, distances of points on the sphere are approximately conserved. Despite this disadvantage the stereographic projection was chosen because it allows for a simple and straightforward interpretation and has a nice geometrical meaning. Note that due to the identification of antipodal MPVs, opposite points on the unit circle in stereographic projection have to be identified. For $l = 2$ the plot already shows one feature that we will encounter in Sect. VIII, namely that the MPVs nearly lie in the plane orthogonal to the Cosmic Dipole.

In App. C further stereographic projection plots for $l = 3, 4$ (Fig. 22) and $l = 48, 49$ (Fig. 23) can be found.

VIII. RESULTS

The four statistics mentioned in Sect. VI were calculated for all four full-sky maps using all test directions and compared to the statistics of one thousand Monte Carlo ensembles of Gaussian and isotropic a_{lm} .

A. Reproduction of known large scale anomalies and investigation of intermediate scales with outer vertical statistic

It has been observed in previous studies, that on largest angular scales, i.e. the quadrupole and octupole, the MPVs correlate with the Cosmic Dipole. Fig. 6a shows that this correlation is due to a strong orthogonality of

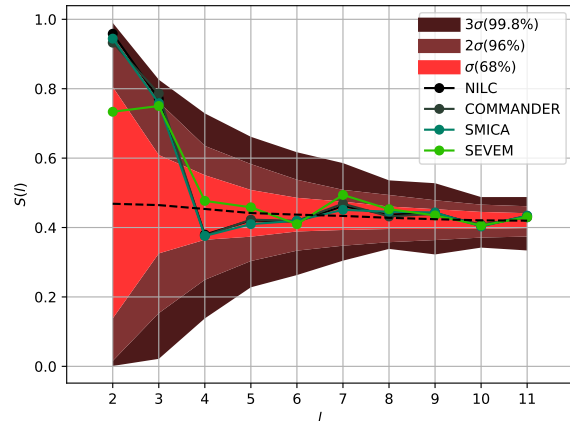
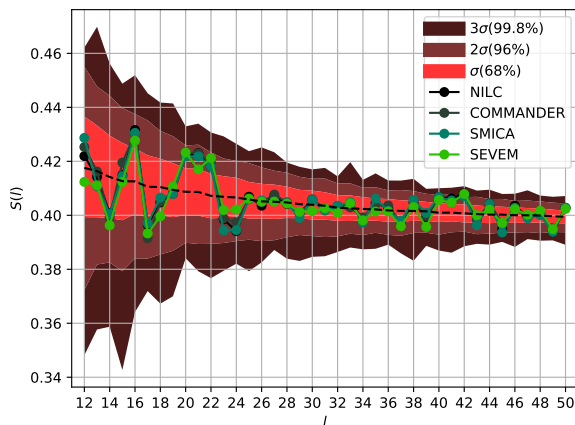
a) Large angular scales $2 \leq l \leq 11$ b) Smaller angular scales $12 \leq l \leq 50$

FIG. 6: Comparison of pipelines for $S_{\mathbf{D}}^v$ with \mathbf{D} the *Cosmic Dipole*. Expectation value and 1, 2, 3 σ regions from Monte Carlo simulations are included.

the MPVs and the Dipole direction. The area vectors of the quadrupole and octupole in COMMANDER, NILC and SMICA show an alignment with the Dipole at 2 σ -level. By visualising the quadrupole as a plane, this means that the Cosmic Dipole direction is nearly perfectly orthogonal to this plane which can not be achieved in about 96% of random ensembles of Gaussian and isotropic temperature fluctuation fields. The quadrupole value of SEVEM seems less anomalous, but as we will argue later, SEVEM still shows strong residual foreground effects and hence should not be considered for full-sky data analysis.

Fig. 6b shows the vertical outer statistic for smaller angular scales. The region $20 \leq l \leq 24$ sticks out just like the largest angular scales. At these scale data points outside the 1 σ -regions cluster. Both scale ranges show a similar behavior; first the MPVs are too close to the plane

orthogonal to the Cosmic Dipole, then they are too far away from this plane. It should be noted that the two suspicious scales (large and intermediate) coincide with the scales at which the measured angular power spectrum deviated from the best-fit Λ CDM model of the Planck 2015 analysis [15]. This hints towards a connection between the power spectrum deviation and the peculiar motion of the Earth with respect to the cosmic frame.

B. Comparison of directions and pipelines using aligned statistics

In Figs. 7 and 9 to 11 we plot the outer statistic $S_{\mathbf{D}}^{\parallel}$ for each of the five directions including the 1 σ - to 3 σ -regions from the Monte Carlo simulations in the range of large angular scales $2 \leq l \leq 11$ and in the range of smaller angular scales $12 \leq l \leq 50$, comparing in each plot all four pipelines. Fig. 12 shows the same for the inner statistic S^{\parallel} . Fig. 8 shows the outer likelihood as a function of l for the Cosmic Dipole.

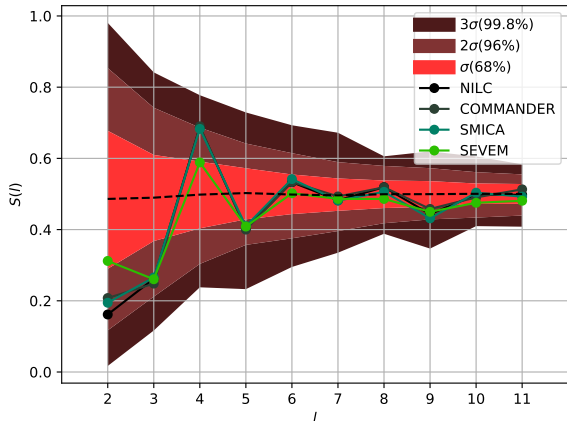
1. Cosmic dipole

One observes, see Fig. 7a, that the large scale anti-correlation of the quadrupole and octupole with the Cosmic Dipole – see for example the review [21] – is still present in the second release data. While for SEVEM the anti-alignment is more pronounced at $l = 2$, both multipole data points are equally unusual in the other three pipelines (both nearly 2 σ). It turns out that for $l = 4$ an even less expected alignment of the COMMANDER, NILC and SMICA data with the Dipole is present. Except for SEVEM each of the lowest multipoles $l = 2, 3, 4, 5$ shows an unexpected behavior with respect to the Cosmic Dipole.

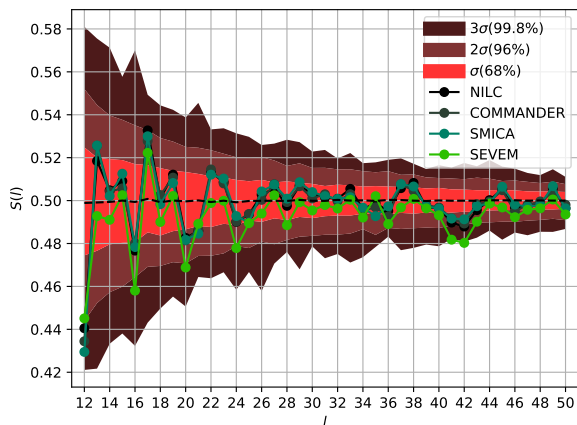
The large multipole behavior, see Fig. 7b, already shows a clear deviation of SEVEM from the other three pipes. On the whole range $12 \leq l \leq 50$ SEVEM is less aligned with the Cosmic Dipole than the other cleaned maps and it admits more unlikely data points. Nine out of 38 data points in this regime are at or even beyond 2 σ , one even beyond 3 σ .

Concerning COMMANDER, SMICA and NILC, all in all 18 out of 49 multipoles are outside of the 1 σ -region, these are: $l = 2, 3, 4, 5, 9, 12, 13, 16, 17, 20, 21, 35, 37, 38, 41, 42, 45$ and 49. Despite the large angular scale $2 \leq 5$ there is no other clustering of at least four unlikely multipoles in a row, but the range $35 \leq l \leq 45$ tends to be a bit conspicuous. Since one would expect approximately 16 multipoles to lie outside of the 1 σ -region, the conclusion here is that for $l \geq 5$ the data follows the statistically expected behavior. Furthermore neither alignment nor anti-alignment is preferred.

Fig. 8 shows the outer likelihoods for the Cosmic Dipole. It is clearly shown that there is a range, $25 \leq$



a) Large angular scales/small multipoles



b) Small angular scales/large multipoles

FIG. 7: Comparison of pipelines for $S_{\mathbf{D}}^{\parallel}$ with \mathbf{D} the *Cosmic Dipole*. Expectation value and 1, 2, 3 σ regions from Monte Carlo simulations are included.

$l \leq 34$, that does not include any unlikely data point regarding the Cosmic Dipole. Hence, we can conclude that the Cosmic Dipole does not have any effect on the data on angular scales of about 5.3 - 7.2 deg. But once again one sees that in the range $20 \leq l \leq 24$ low likelihoods cluster. Comparing the two statistics $S_{\mathbf{D}}^v$ and $S_{\mathbf{D}}^{\parallel}$ one sees that the contribution to low likelihoods mainly stems from the vertical statistic.

Eventually we state that COMMANDER, NILC and SMICA show a very similar behavior and deviate less from each other than one would naively expect. It seems that the cleaning algorithms (except for SEVEM) all have the same quality on the considered range of scales and that the precise choice of the cleaning algorithm does not affect the results. Since the three algorithms use different frequency bands and different masks the strong coincidence surprises.

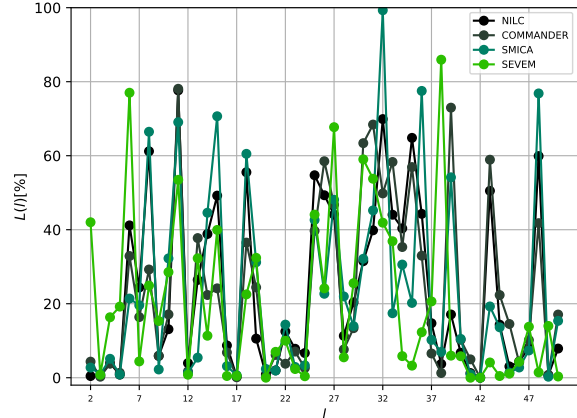


FIG. 8: Comparison of outer likelihoods in dependence of l for the range $2 \leq l \leq 50$ and the Cosmic Dipole as the outer direction.

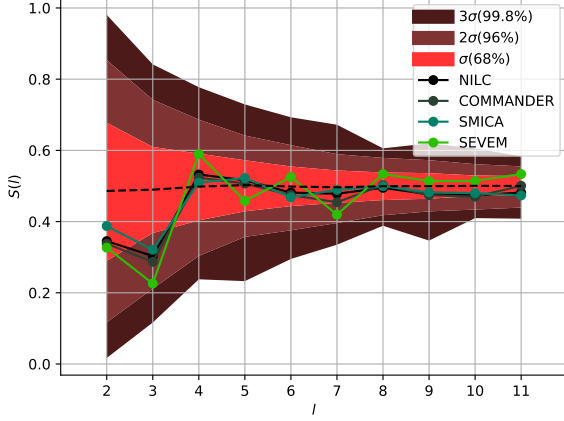
2. Galactic pole

Apart from the quadrupole $l = 3$ the large scale behavior of the Galactic Pole is as expected (even in the SEVEM map), see Fig. 9a. When referring to larger multipoles, see Fig. 9b, SEVEM shows even stronger deviations from the other maps than in the other directions. From $l = 12$ on SEVEM is tremendously aligned with the Galactic Pole. Eight out of 39 data points lie even outside of the 3 σ -region. Again, this behavior is expected, since the residuals of the Milky Way still have a large impact on SEVEM. Hence, one concludes that SEVEM cannot be used for cosmological analyses that make use of the whole sky, particularly MPV analysis.

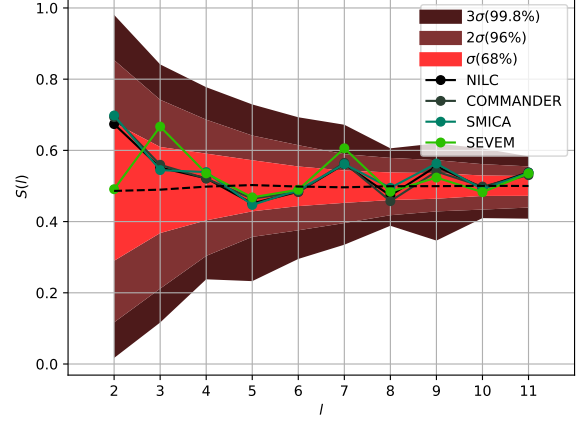
Concerning the other maps neither alignment nor anti-alignment is preferred. The unusual larger multipoles are $l = 13, 14, 16, 23, 24, 25, 31, 35, 37, 38, 40, 41, 42$ and 46, where $l = 14$ and 16 are the most unusual ones. On the whole observed range this yields 15 multipoles outside of 1 σ which again is allowed by statistics.

When comparing Fig. 9 to Fig. 24a from App. C, where statistic $S_{\mathbf{D}}^{\parallel}$ is plotted for the Galactic Pole for all four pipelines but with the SEVEM mask applied to the map, it becomes obvious that the strong alignment of SEVEM with the Galactic Pole is solely due to the masked region. When the mask is applied, all four maps show a similar behavior and the deviation of SEVEM from the others vanishes nearly completely, especially in the high l regime. This is not surprising since it is assumed by the Planck Collaboration itself that SEVEM carries residual effects of the Galactic Plane.

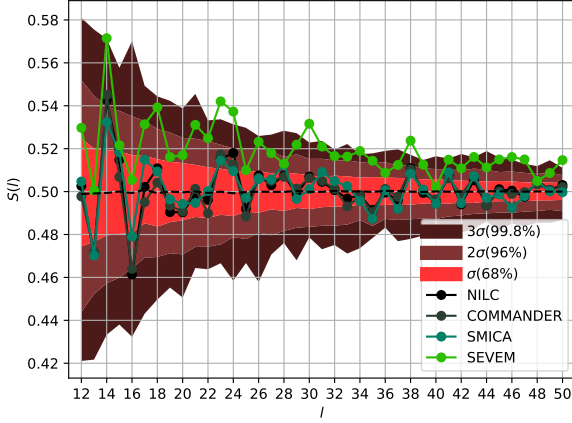
Altogether, on the whole range $2 \leq l \leq 50$ the Galactic Pole incorporates more low probability multipoles than the Galactic Center or the Ecliptic Pole but approximately as many as the Cosmic Dipole.



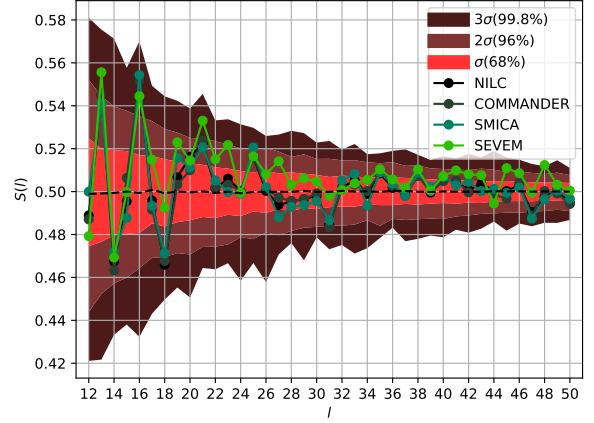
a) Large angular scales/small multipoles



a) Large angular scales/small multipoles



b) Small angular scales/large multipoles



b) Small angular scales/large multipoles

FIG. 9: Comparison of pipelines for $S_{\mathbf{D}}^{\parallel}$ with \mathbf{D} the *Galactic Pole*. Expectation value and 1, 2, 3 σ regions from Monte Carlo simulations are included.

3. Galactic center

The behavior with respect to the Galactic Center tends to be less unexpected than the Cosmic Dipole on large angular scales, see Fig. 10a. Only $l = 2, 7$ and 9 lie just outside of 1σ . Again SEVEM deviates clearly from the other maps on smaller angular scales, see Fig. 10b, this time showing a stronger alignment with the Galactic Center, especially on the mid-range scales which correspond approximately to the angular size of the galactic core.

The unlikely higher multipoles of the other maps are $l = 13, 14, 16, 18, 21, 25, 27, 31, 33, 47$ and 50 , yielding again a total of 14 points outside of 1σ on the whole range, which is completely allowed by our assumption. Let us remark, that especially on smaller scales it seems that anti-alignment with the Galactic Center is preferred

FIG. 10: Comparison of pipelines for $S_{\mathbf{D}}^{\parallel}$ with \mathbf{D} the *Galactic Center*. Expectation value and 1, 2, 3 σ regions from Monte Carlo simulations are included.

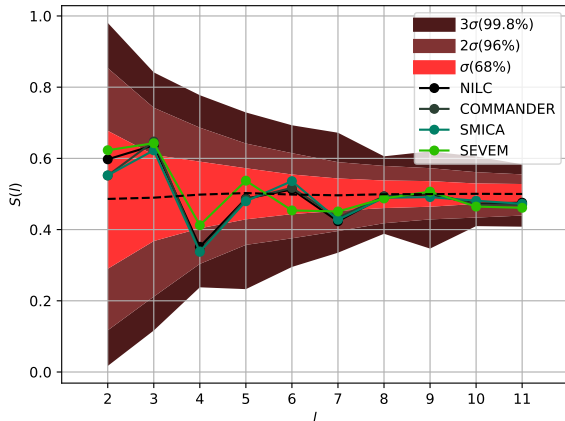
a bit compared to alignment.

It attracts attention that there are three multipoles far away from the expectation in the non-SEVEM maps. The multipoles $l = 16, 18$ and 47 have data points outside of the 2σ -regions – that means one point more than expected – and $l = 16$ is nearly at 3σ . Compared to the Cosmic Dipole the Galactic Center shows fewer low probability data points, but in turn it shows more data points outside the 2σ -region.

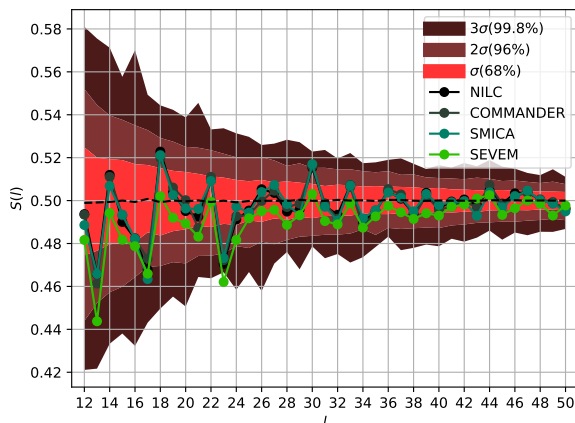
4. Ecliptic pole

On large angular scales, see Fig. 11a, the data shows an even more expected behavior with respect to the Ecliptic Pole than with respect to the Cosmic Dipole. Neverthe-

5. Inner alignment



a) Large angular scales/small multipoles



b) Small angular scales/large multipoles

FIG. 11: Comparison of pipelines for $S_{\mathbf{D}}^{\parallel}$ with \mathbf{D} the *Ecliptic Pole*. Expectation value and 1, 2, 3 σ regions from Monte Carlo simulations are included.

less $l = 3, 4$, and 7 are outside of the 1σ -region.

On smaller angular scales, see Fig. 11b, SEVEM again clearly deviates from the other maps, showing more anti-alignment with the *Ecliptic Pole*. The other maps have data points outside the 1σ -region for $l = 13, 17, 18, 23, 30, 34, 43$ and 50 . Together with the conspicuous large scale multipoles altogether 11 out of 49 data points lie outside 1σ which is even less than the expected 16. Comparing this to the *Cosmic Dipole* alignment one observes that both directions share unusual values of the alignment statistic at $l = 3, 4, 13$, but the rest of the points is shifted. Furthermore, the *Ecliptic* seems to have less impact on the CMB data than the *Dipole*.

The inner statistic S^{\parallel} comes equipped with a much smaller variance than the outer statistic $S_{\mathbf{D}}^{\parallel}$, as can be seen in Fig. 12. Hence, the inner statistic is more susceptible to computational errors or minor fluctuations than the outer statistic, but nevertheless the plots paint a distinct picture: The inner statistic of COMMANDER, NILC and SMICA lies inside 1σ for most of the multipoles and does not leave 2σ one single time. No strong outliers are present, neither in the low l - nor in the large l regime. If anomalies are present in the CMB, they seem to be mainly caused by correlation with outer directions, while no remarkable intra-multipole correlation is present. Note, that other methods than ours could reveal hidden intra-multipole correlations that cannot be observed with our simple method.

C. Comparison of directions using likelihood histograms

By plotting histograms for likelihoods $0\% \leq L \leq 100\%$ for the real CMB full sky data and comparing it to the expectation from Gaussian and isotropic Monte Carlo, see Fig. 4 in Sect. VI, we receive a measure of anisotropy on the whole range $2 \leq l \leq 50$ which is more precise than the estimates above where we just counted multipoles outside of 1σ but without taking into account their individual p-values. Furthermore, by combining two statistics into one likelihood compresses the information content.

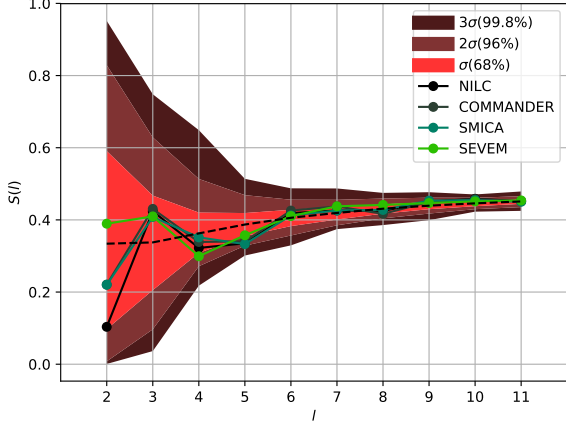
1. SEVEM

The large deviations from the expectation, that have been observed by investigating the alignment statistics alone, can be seen more easily from the likelihood histograms of the inner likelihood, see Fig. 13, and the outer likelihood, see Fig. 14.

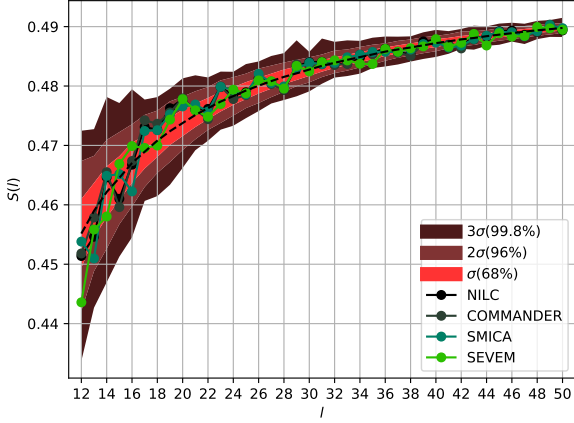
The bins $0 - 10$, $10 - 20$, $20 - 30$, $30 - 40$, $50 - 60$ and $60 - 70$ in Fig. 13 lie outside 1σ . The bin of lowest likelihoods $0 - 10$ reaches nearly 2σ . Hence, SEVEM's inner statistics incorporate too much data points with likelihoods of at most 10%. 12 out of 49 data points result in low likelihoods, which is unexpected.

SEVEM's strange behavior becomes even more pronounced when considering the outer likelihoods, see Fig. 14. While the *ecliptic pole* and the *Cosmic Dipole* show a relatively normal behavior, the *Galactic Center* and especially the *Galactic Pole* are far off the expectation. Altogether, 33 out of 49 values for the *Galactic Pole* have a likelihood which is smaller than 10%.

Hence, we can conclude, that SEVEM shows a slight anomaly with respect to intra multipole correlations, while it shows an enormous anomaly with respect to outer correlations with the *Galactic Center* and most



a) Large angular scales/small multipoles



b) Small angular scales/large multipoles

FIG. 12: Comparison of pipelines for S^{\parallel} . Expectation value and 1, 2, 3 σ regions from Monte Carlo simulations are included.

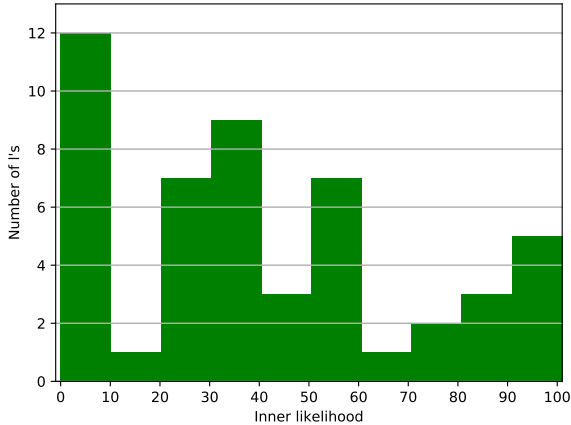


FIG. 13: Inner likelihood histogram for SEVEM.

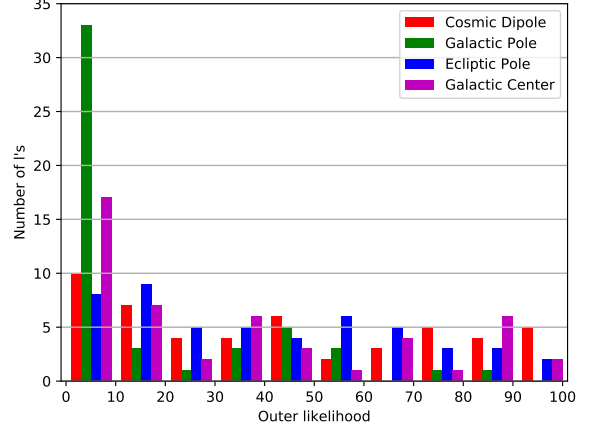


FIG. 14: Outer likelihood histogram for SEVEM.

strongly with the Galactic Pole, whose statistics correspond to measures of the influence of the Galactic Plane. The combination of the Galactic Pole and Center anomalies evokes the conjecture, that SEVEM is mainly influenced and strongly polluted by the Milky Way.

Note, that also the number of low likelihoods in the Dipole direction is slightly above what statistics tells us, but it is overshadowed by the large impact of the Galactic directions. We will see below that the Dipole is the most conspicuous direction in the other three maps, but which is mainly induced by the four multipoles $l = 2, 3, 4, 5$ and partly but weaker by $l = 20, 21, 22, 23, 24$.

2. NILC

Now, we exclude SEVEM and only consider the other three maps COMMANDER, NILC and SMICA. It turns out, as already conjectured in the investigation of the pure statistics, that all three maps deviate only marginally. While COMMANDER tends to be the map with slightly larger likelihoods than the other two maps, NILC is equipped with the smallest confidence mask and therefore we choose to present only the NILC results and mention, that COMMANDER seems to be closer to the expectation while SMICA is slightly further away than NILC. Here again the striking similarity of all three maps, despite their very different cleaning procedures, is quite remarkable.

The overall structure of inner likelihoods, see Fig. 15, is remarkably normal except for the fact that the number of lowest likelihoods is even smaller than expected (even nearly 2σ). It seems that some artificial intra-multipole isotropy could have been induced in the course of data processing, resulting in a lack of variance in intra-multipole correlations. Apart from this, the inner likelihoods do not show any further noticeable feature.

The aligned likelihood, see Fig. 16, shows expected be-

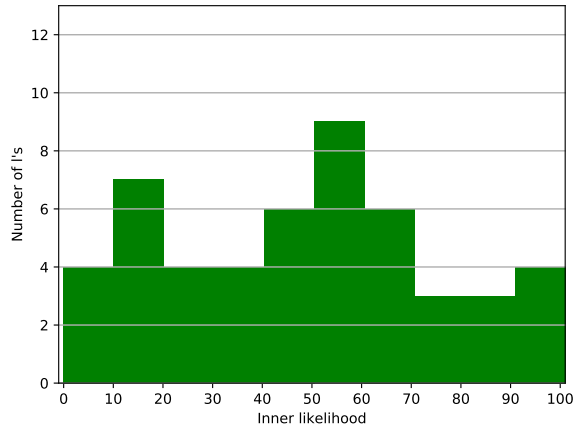


FIG. 15: Inner likelihood histogram for NILC.

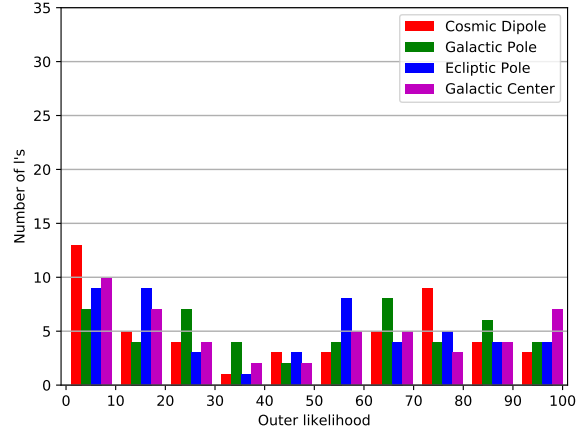


FIG. 17: Outer likelihood histogram for NILC.

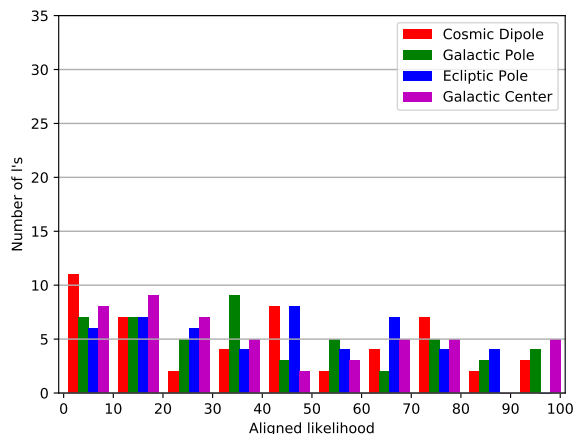


FIG. 16: Aligned likelihood histogram for NILC.

behavior for all directions but the Cosmic Dipole. The number of multipoles with aligned likelihoods less than 10% for the Cosmic Dipole as outer direction is higher than one would expect from a Gaussian and isotropic set of a_{lm} . The sign is weaker as for the outer likelihood. The reason for this is that though the inner likelihood stems from two non-correlating statistics, it is not a good measure for possible violation of isotropy due to the cancellation of unusual outer behavior by the highly isotropic inner statistics. The aligned likelihood underestimates the effects of outer directions by mixing inner and outer information.

Therefore one should focus on the outer likelihood. The correlation of the two statistics, that are used to build this likelihood, does not reveal itself in the histograms, hence the histograms describe a measure for anisotropies that is not sensitive to the correlation of the used statistics. Fig. 17 shows that the lowest likelihood bin (0-10) is filled up to exactly 2σ in the Dipole direc-

tion, while all other directions are inside of 1σ . On average NILC is not strongly influenced by the Milky way on the considered multipole range.

3. Parity

Eventually, let us investigate a possible parity asymmetry. Considering the outer likelihoods of NILC for even and odd multipoles, see Fig.18, we see that a parity transform effects the Galactic Center most, while the Cosmic Dipole and Galactic Pole are nearly unaltered. Galactic Center and Ecliptic Pole likelihoods get shifted to lower values when transitioning from even to odd modes. Altogether, odd modes are slightly less probable than even modes. Nevertheless, when plotting the likelihoods of even and odd modes in dependence of l separately, no clearly distinguishable pattern can be observed. Still both plots show an oscillatory behavior, which implies that in addition a more complicated asymmetry pattern in addition to a parity asymmetry concerning Galactic Center is present in the data.

The slight influence of parity in the outer statistics of the galactic center is partly expected since it naturally distinguishes a parity.

IX. DISCUSSION

We find that SEVEM strongly deviates from COMMANDER, NILC and SMICA in every regard. It is strongly aligned with the Galactic Center and the Galactic Pole and strongly anti-aligned with the Dipole and the Ecliptic Pole in the S_D^{\parallel} statistic. The alignment with the Galactic Center is most prominent on mid-range multipoles, indicating a strong pollution from the Galactic Core that has not been removed in the cleaning process. Furthermore, the deviation of SEVEM from the other

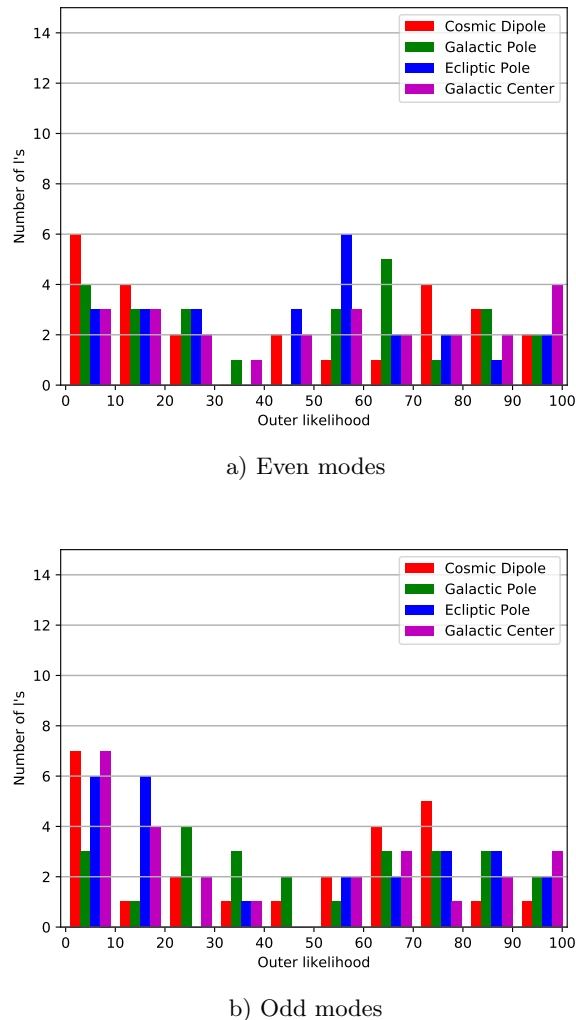


FIG. 18: Outer likelihood histograms for NILC for even and odd multipoles.

maps is most present at $l \leq 12$, which indicates that the central part of the Milky Way is the dominating source of distraction in SEVEM. Using SEVEM in all sky analyses always carries residual Milky Way effects. Hence, SEVEM should not be used for analysis of isotropy, unless one focuses on certain patches outside the critical area and uses a mask. Nevertheless, the correlation with the Cosmic Dipole, that is present in the other maps, could also be seen in SEVEM. It is just overshadowed by the sizable galactic residuals. Since none of the above observations surprised, SEVEM serves us as a control map. The fact that we were able to identify the expected residual foreground features of SEVEM with our method shows that our method yields geometrically easily interpretable results and that the heuristic geometric intuition of the used statistics is correct. Hence, the outer statistics truly measure the influence of the given directions that are included.

COMMANDER, NILC and SMICA show a surprisingly similar behavior, deviating only marginally on the observed range. While with respect to the Galactic Center and Pole and the Ecliptic Pole the data does not show abnormal statistical behavior, a correlation with the Cosmic Dipole is visible, concentrating mainly on largest angular scales $2 \leq l \leq 5$ and on intermediate scales $l = 20, 21, 22, 23, 24$. The behavior of the aligned statistic shows an analogue scheme at both ranges, first there is anti-alignment, then alignment.

Intra-multipole correlations are underrepresented in the data because a lack of variance can be observed resulting in a lack of low likelihoods. Hence, it could be that data processing induces artificial isotropy into the central belt.

The correlation with the Cosmic Dipole at the lowest multipoles is present both in anti-alignment ($l = 2, 3, 5$) and alignment ($l = 4$), but also the range $35 \leq l \leq 45$ seems slightly conspicuous, while the range $25 \leq l \leq 34$ is surprisingly normal with absence of small likelihoods. The large scale (anti-)alignments imply that we do not yet fully understand the true nature of the Dipole, i.e. the relative motion of the Solar System with respect to the Cosmic Frame. Since these anomalies are present in all of the maps such a physical origin could be more likely than data processing reasons.

The multipole $l = 13$ sticks out, since it is equipped with a low probability in each of the maps and concerning each direction. The quadrupole is present in three of the directions, and for example the regions $12 \leq l \leq 14$ and $16 \leq l \leq 18$ are pronounced in at least one of their multipoles in each direction.

We find a weak hint that the parity anomaly of the CMB could be caused mainly by processes connected with the Galactic Center, so we suggest foreground reasons for those.

X. CONCLUSION

We gave an overview over different extraction methods for multipole vectors. MPVs can be represented via a symmetric and trace-free tensor applied to the symmetric and trace-free product of unit vectors, which yields an algorithm for extracting MPVs from the spherical harmonic decomposition. Alternatively methods from algebraic geometry can be used to identify MPVs as lines in \mathbb{CP}^2 . A third approach uses the extension of the Bloch sphere to higher spin and the stereographic projection. The resulting polynomial can be understood as the scalar product of a spin state with Bloch coherent states. The latter approach can be used to assign joint probability densities to MPVs. It turns out that the explicit expression for the joint probability density is the same for the set of all distributions of completely random a_{lm} . This set forms a subset of statistical isotropic distributions and the intersection of completely random and Gaussian distributions yields the regime of standard cosmology.

Using different simple statistics we observed numerically a correlation of the full sky cleaned maps with the Cosmic Dipole on the largest angular scales $2 \leq l \leq 5$ and intermediate angular scales $l = 20, 21, 22, 23, 24$. These are the same multipole numbers which also deviate from the theoretical expectation in the angular power spectrum. Furthermore we have observed, that artificial isotropy is induced inside of multipoles visible in the form of a lack of variance of inner statistics, which might or might not be a remnant of data processing. The SEVEM map is still strongly polluted by the Galactic foreground.

In the future, one could also study cross-multipole correlations on the observed range of scales and investigate if the previously observed large scale correlations precede down to smaller scales.

Furthermore one needs more insight about possible physical reasons for CMB anomalies. One should especially focus on detailed studies of the Dipole and reveal its true nature.

Apart from the large ($l = 2, 3, 4$) and intermediate ($l = 20, 21, 22, 23, 24$) scale Dipole anomalies we could not find any prominent violations of statistical isotropy on angular scales of about $3.6 \text{ deg} \leq \theta \leq 30 \text{ deg}$.

ACKNOWLEDGMENTS

We acknowledge financial support by the DFG Research Training Group 1620 *Models of Gravity*. Furthermore we would like to thank Craig Copi for the multipole vector calculation program [32] that we used, and Ger not Akemann for useful discussions and an insight about random matrix theory.

This work is based on observations obtained with Planck (<http://www.esa.int/Planck>), an ESA science mission with instruments and contributions directly funded by ESA Member States, NASA, and Canada.

The results in this paper have been derived using the HEALPix [44] package and especially the HEALPy implementation for python.

Appendix A: Derivation of one-point density

For $l = 1$ we get from (39)

$$\begin{aligned} p_1\left(\zeta, \frac{-1}{\zeta^*}\right) &= \frac{1}{\pi} \frac{1}{|\zeta|^2} \frac{\left|\zeta + \frac{1}{\zeta^*}\right|}{\left((1 + |\zeta|^2)(1 + |1/\zeta^*|^2) + (1 + \zeta(-1/\zeta^*)^*) \underbrace{(1 - \zeta^*/\zeta^*)}_{=0} \right)^{3/2}} \\ &= \frac{1}{\pi} \frac{1}{|\zeta|} \frac{\left(1 + \frac{1}{|\zeta|^2}\right)}{\left((1 + |\zeta|^2) \left(1 + \frac{1}{|\zeta|^2}\right) \right)^{3/2}} = \frac{1}{\pi} \frac{1}{|\zeta|^3} \frac{(1 + |\zeta|^2)}{\left((1 + |\zeta|^2) \left(1 + \frac{1}{|\zeta|^2}\right) \right)^{3/2}} \\ &= \frac{1}{\pi} \frac{(1 + |\zeta|^2)}{(1 + |\zeta|^2)^3} = \frac{1}{\pi} \frac{1}{(1 + |\zeta|^2)^2}. \end{aligned}$$

Using $\zeta = \tan(\theta/2) \exp(i\phi)$ we receive

$$\begin{aligned} \left| \left(\frac{\partial(\zeta, \zeta^*)}{\partial(\theta, \phi)} \right) \right| &= \tan(\theta/2)(1 + \tan^2(\theta/2)) \\ \Rightarrow d\zeta d\zeta^* &= \frac{\tan(\theta/2)(1 + |\zeta|^2)}{\sin(\theta)} d\Omega \\ \Leftrightarrow d\Omega &= \frac{2 \sin(\theta/2) \cos(\theta/2)}{\tan(\theta/2)} \frac{d\zeta d\zeta^*}{1 + |\zeta|^2} = 2 \cos^2(\theta/2) \frac{d\zeta d\zeta^*}{1 + |\zeta|^2} = \frac{1}{1 + \tan^2(\theta/2)} \frac{d\zeta d\zeta^*}{1 + |\zeta|^2} \\ &= \frac{2d\zeta d\zeta^*}{(1 + |\zeta|^2)^2}, \end{aligned}$$

with $d\Omega = \sin(\theta) d\theta d\phi$ and $\left| \left(\frac{\partial(\zeta, \zeta^*)}{\partial(\theta, \phi)} \right) \right|$ the Jacobi determinant of the change of coordinates. Hence we have

$$\begin{aligned} p_1(\theta, \phi) d\Omega &= p_1(\theta, \phi) \frac{2d\zeta d\zeta^*}{(1 + |\zeta|^2)^2} \stackrel{!}{=} p_1(\zeta, -1/\zeta^*) d\zeta d\zeta^* = \frac{1}{\pi} \frac{d\zeta d\zeta^*}{(1 + |\zeta|^2)^2} \\ \Rightarrow p_1(\theta, \phi) &= \frac{1}{2\pi}. \end{aligned}$$

Appendix B: Joint Probability Distribution of Multipole Vectors: Connection to Gaussian analytic functions and random matrix theory

The Majorana polynomial in (26) is a special case of the wide class of Gaussian analytic functions (GAFs), see

[49]. In general, a GAF is defined as a random field on \mathbb{C}^n

such that for each z_1, \dots, z_n the quantity $f(z_1, \dots, z_n)$ is a normally distributed random variable.

For every $L \in \mathbb{N}$ the function

$$f(z) = \sum_{n=0}^L \sqrt{\binom{L}{L-n}} a_n z^n, \quad (\text{B1})$$

with identically and independently distributed zero mean and unit variance complex random variables a_n is a GAF whose zero set is invariant under the action of $\text{SO}(3)$. Its covariance kernel is given by $\text{Cov}(f(z), f(w)) = K(z, w) = (1 + zw^*)^L$. The Majorana polynomial equals this GAF up to a factor $(-1)^l$ which can be combined into Ψ_m , and with $L = 2l$ and substituting $n = m + l$, yielding $\Psi_m = a_{m+l}$. The Ψ_m do not have unit variance, but variance C_l . By rescaling Ψ_m a common factor for all Ψ_m can be pulled out of the sum. This does not change the behavior of the zeros.

The general density (35) holds for every GAF, while the one-point density (40) can be expressed as

$$p_1(z) = \Delta \log(K(z, z))/4\pi, \quad (\text{B2})$$

for a general GAF. This equals – up to a different normalization – the one-point density of the Majorana polynomial in \mathbb{C} which was used in the proof of (40). The formula above is known as *Edelman-Kostlan formula*, see [50].

One can show that one-point statistics, which are compactly supported, are asymptotically normal regarding rotationally invariant GAFs. Let $\phi \in \mathcal{C}_c^2(\Lambda)$ and

$$\mathcal{L}_L(\phi) := \sum_{z \in f^{-1}(0)} \phi(z), \quad (\text{B3})$$

then the following asymptotic behavior is valid:

$$\sqrt{L}(\mathcal{L}_L(\phi) - \langle \mathcal{L}_L(\phi) \rangle) \xrightarrow{l \rightarrow \infty, \text{distribution}} N(0, \kappa(\phi)), \quad (\text{B4})$$

where $\kappa(\phi)$ denotes some number that depends on the function ϕ . Unfortunately, the above is a priori not true for functions ϕ with arbitrary support. Hence, it does not apply to the statistics in Sect. VI. Since we are dealing with one hemisphere, one could restrict the scalar products appearing in those statistics to the unit disc. This cutoff compactifies the statistic but unfortunately it destroys any kind of differentiability. Nevertheless the result above could be used to study local statistics on certain patches on the sky in the large l limit in future investigations.

Remember that the Majorana polynomial has covariance kernel $K(z, w) = (1 + zw^*)^{2l}$. The following statement will show that MPVs as zeros of the isotropic GAF and eigenvectors of Gaussian random matrices are tightly connected: Let A, B be independent $(n \times n)$ random matrices with identically and independently distributed complex standard Gaussian entries. Then the eigenvalues of $A^{-1}B$ form a determinantal point process on \mathbb{C}

with covariance kernel $K(z, w) = (1 + zw^*)^{n-1}$ with respect to the measure $n/(\pi(1 + |z|^2)^{n+1}) \cdot dm(z)$ and the eigenvectors are distributed as

$$p(\{z_i\}) = \frac{1}{n!} \left(\frac{n}{\pi}\right)^n \prod_{k=1}^n \frac{\prod_{i < j} |z_i - z_j|^2}{(1 + |z_k|^2)^{(n+1)}} \quad (\text{B5})$$

according to the Lebesgue measure on \mathbb{C}^n .

One can see that the covariance kernel of these eigenvalues and the covariance kernel of the Majorana polynomial are equal for $n = 2l + 1$ and that the probability density above and the one in (39) look similar, but still different. The reason for this difference is of course that the zeros of the spherical GAF do not follow a determinantal process, but rather some kind of permanent process. In fact, the only case of a GAF whose zero set is known to follow a determinantal process is the following one:

$$f(z) = \sum_{n=0}^{\infty} a_n z^n. \quad (\text{B6})$$

This is a special case of a hyperbolically invariant GAF and there are some striking results considering this special function. Unfortunately, the rotationally invariant GAF has not yet been confirmed to imply a determinantal process.

A better understanding of the possible relationship between Gaussian random matrices and MPVs would help in investigating CMB anomalies with MPVs. Two-point functions of eigenvalues are known simple expressions while in principle the joint probability density of the MPVs (35) is computable as well.

Appendix C: Additional Plots

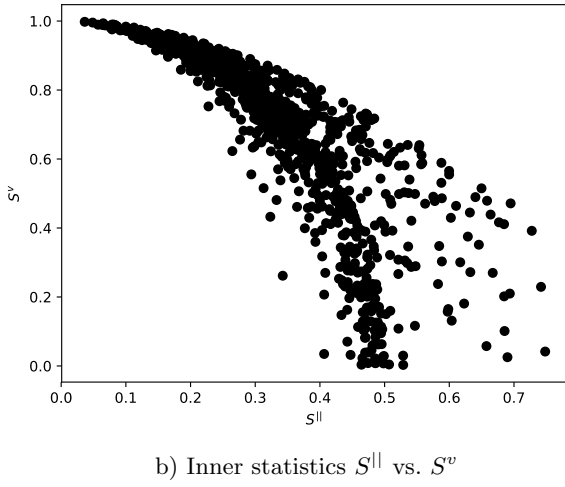
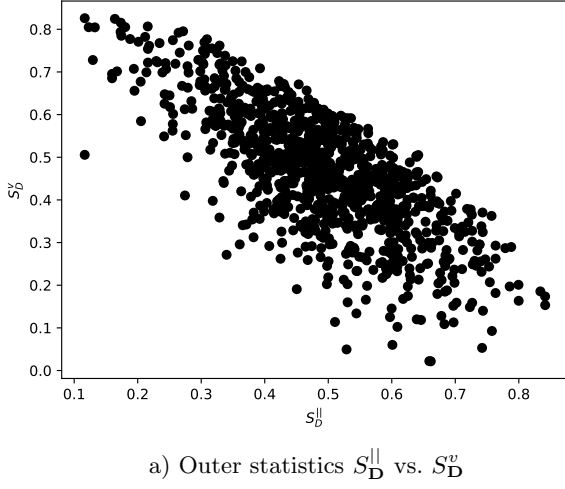


FIG. 19: Correlation of statistics for $l = 3$

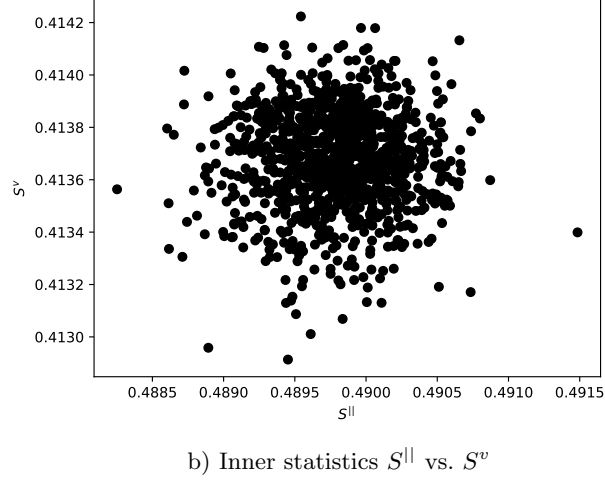
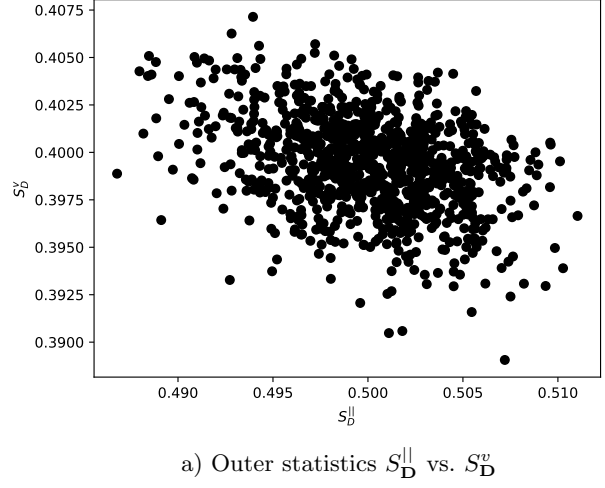
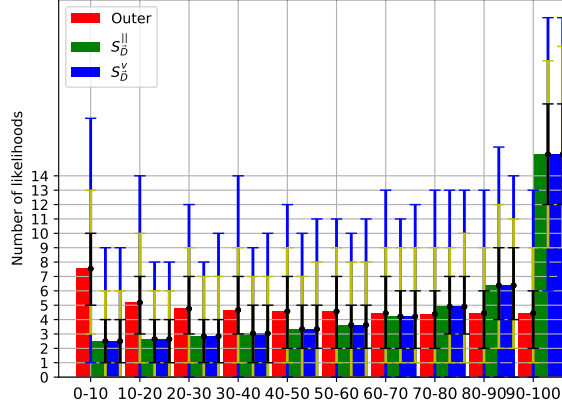
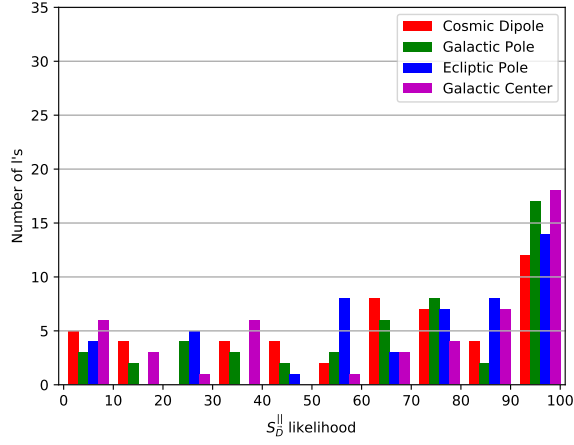


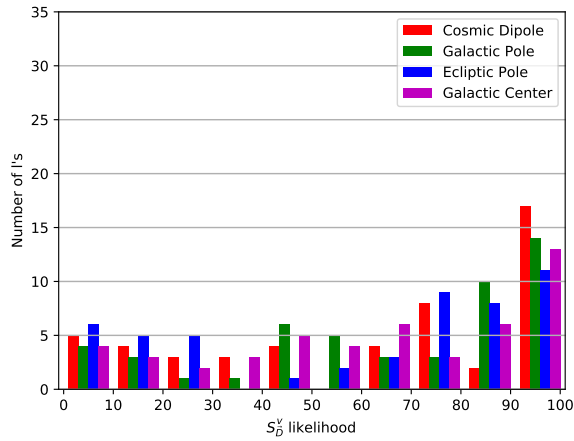
FIG. 20: Correlation of statistics for $l = 50$



a) Comparison of isotropic and Gaussian expectation of histograms of outer likelihood and likelihoods with only $S_D^||$ and S_D^v included.

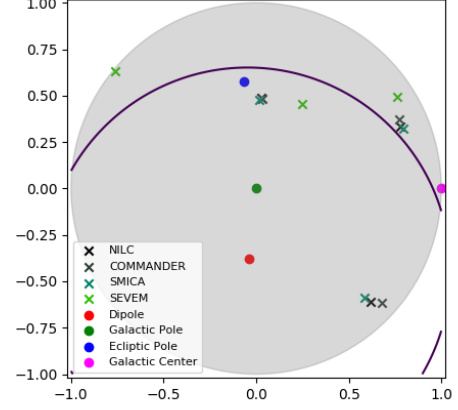


b) NILC histogram of likelihood where only the statistic $S_D^||$ has been taken into account.

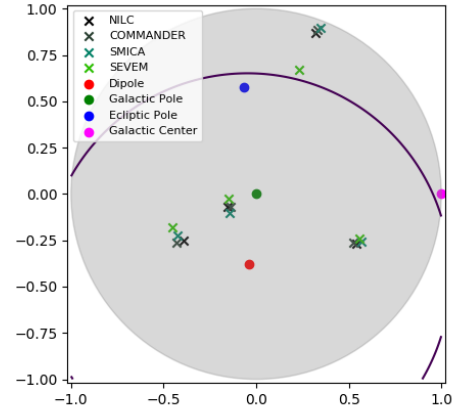


c) NILC histogram of likelihood where only the statistic S_D^v has been taken into account.

FIG. 21: Histograms of likelihoods that include only a single statistic.



a) $l = 3$



b) $l = 4$

FIG. 22: Multipole vectors and physical directions in stereographic projection. The violet curve shows the plane orthogonal to the Cosmic Dipole.

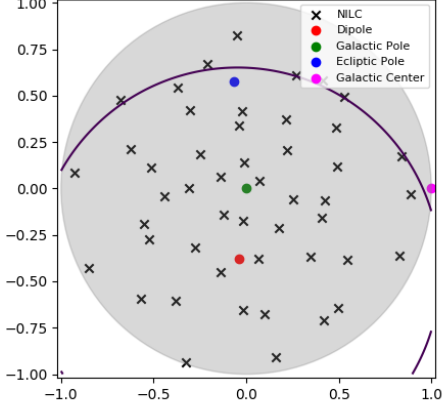
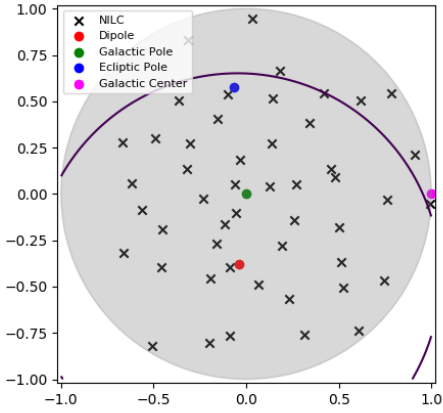
a) $l = 48$ b) $l = 49$

FIG. 23: Multipole vectors (only NILC) and physical directions in stereographic projection. The violet curve shows the plane orthogonal to the Cosmic Dipole. $S_{\vec{D}}^{\parallel}$ with \vec{D} the Cosmic Dipole is especially normal at $l = 48$ (inside 1σ -region close to expectation) and especially unusual at $l = 49$ (alignment, outside 1σ , inside 2σ).

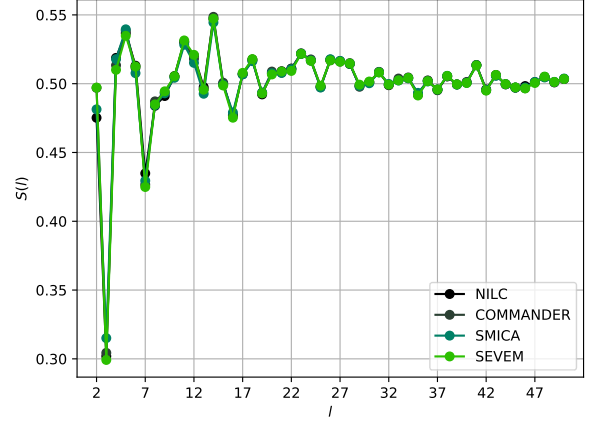
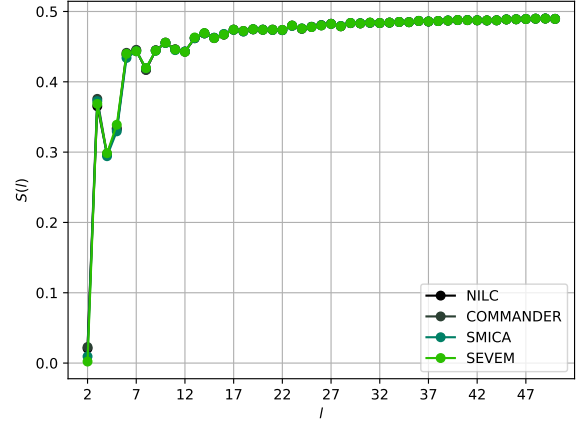
a) $S_{\vec{D}}^{\parallel}$ with \vec{D} the Galactic Poleb) S^{\parallel}

FIG. 24: Aligned statistics for the Planck data with SEVEM mask applied and without Monte Carlos from $l = 2$ to $l = 50$. Once the galactic center is properly masked, all four foreground cleaned maps agree very well with each other. The strong deviation of the aligned statistics from the generic expectation for small l is due to the mask, which is the reason why masked maps cannot be used for the analysis of statistical isotropy of the lowest multipole moments.

- [1] C. L. Bennett, M. Halpern, G. Hinshaw, N. Jarosik, A. Kogut, M. Limon, S. S. Meyer, L. Page, D. N. Spergel, G. S. Tucker, E. Wollack, E. L. Wright, C. Barnes, M. R. Greason, R. S. Hill, E. Komatsu, M. R. Nolta, N. Odegard, H. V. Peiris, L. Verde, and J. L. Weiland, *Astrophys. J. Suppl.* **148**, 1 (2003), arXiv:astro-ph/0302207.
- [2] A. de Oliveira-Costa, M. Tegmark, M. Zaldarriaga, and A. Hamilton, *Phys. Rev. D* **69**, 063516 (2004), arXiv:astro-ph/0307282.
- [3] D. J. Schwarz, G. D. Starkman, D. Huterer, and C. J. Copi, *Phys. Rev. Lett.* **93**, 221301 (2004), arXiv:astro-ph/0403353 [astro-ph].
- [4] H. K. Eriksen, F. K. Hansen, A. J. Banday, K. M. Gorski, and P. B. Lilje, *Astrophys. J.* **605**, 14 (2004), [Erratum: *Astrophys. J.* 609,1198(2004)], arXiv:astro-ph/0307507 [astro-ph].
- [5] F. K. Hansen, P. Cabella, D. Marinucci, and N. Vittorio, *Astrophys. J.* **607**, L67 (2004), arXiv:astro-ph/0402396 [astro-ph].
- [6] R. C. Helling, P. Schupp, and T. Tesileanu, *Phys. Rev. D* **74**, 063004 (2006), arXiv:astro-ph/0603594 [astro-ph].
- [7] C. Copi, D. Huterer, D. Schwarz, and G. Starkman, *Phys. Rev. D* **75**, 023507 (2007), arXiv:astro-ph/0605135 [astro-ph].
- [8] H. K. Eriksen, A. J. Banday, K. M. Gorski, F. K. Hansen, and P. B. Lilje, *Astrophys. J.* **660**, L81 (2007), arXiv:astro-ph/0701089 [astro-ph].
- [9] C. J. Copi, D. Huterer, D. J. Schwarz, and G. D. Starkman, *Mon. Not. Roy. Astron. Soc.* **399**, 295 (2009), arXiv:0808.3767 [astro-ph].
- [10] J. Kim and P. Naselsky, *Astrophys. J.* **714**, L265 (2010), arXiv:1001.4613 [astro-ph.CO].
- [11] C. J. Copi, D. Huterer, D. J. Schwarz, and G. D. Starkman, *Adv. Astron.* **2010**, 847541 (2010), arXiv:1004.5602 [astro-ph.CO].
- [12] C. L. Bennett, R. S. Hill, G. Hinshaw, D. Larson, K. M. Smith, J. Dunkley, B. Gold, M. Halpern, N. Jarosik, A. Kogut, E. Komatsu, M. Limon, S. S. Meyer, M. R. Nolta, N. Odegard, L. Page, D. N. Spergel, G. S. Tucker, J. L. Weiland, E. Wollack, and E. L. Wright, *Astrophys. J. Suppl.* **192**, 17 (2011), arXiv:1001.4758 [astro-ph.CO].
- [13] E. Komatsu, *Class. Quant. Grav.* **27**, 124010 (2010), arXiv:1003.6097 [astro-ph.CO].
- [14] E. Komatsu *et al.* (WMAP Science Team), *PTEP* **2014**, 06B102 (2014), arXiv:1404.5415 [astro-ph.CO].
- [15] R. Adam *et al.* (Planck), *Astron. Astrophys.* **594**, A1 (2016), arXiv:1502.01582 [astro-ph.CO].
- [16] P. A. R. Ade *et al.* (Planck), *Astron. Astrophys.* **594**, A13 (2016), arXiv:1502.01589 [astro-ph.CO].
- [17] P. A. R. Ade *et al.* (Planck), *Astron. Astrophys.* **594**, A17 (2016), arXiv:1502.01592 [astro-ph.CO].
- [18] P. A. R. Ade *et al.* (Planck), *Astron. Astrophys.* **594**, A16 (2016), arXiv:1506.07135 [astro-ph.CO].
- [19] R. Adam *et al.* (Planck), *Astron. Astrophys.* **594**, A9 (2016), arXiv:1502.05956 [astro-ph.CO].
- [20] R. Adam *et al.* (Planck), (2015), arXiv:1502.01588 [astro-ph.CO].
- [21] D. J. Schwarz, C. J. Copi, D. Huterer, and G. D. Starkman, *Class. Quant. Grav.* **33**, 184001 (2016), arXiv:1510.07929 [astro-ph.CO].
- [22] P. J. E. Peebles and D. T. Wilkinson, *Phys. Rev.* **174**, 2168 (1968).
- [23] C. Blake and J. Wall, *Nature (London)* **416**, 150 (2002), arXiv:astro-ph/0203385.
- [24] A. K. Singal, *Astrophys. J.* **742**, L23 (2011), arXiv:1110.6260 [astro-ph.CO].
- [25] M. Rubart and D. J. Schwarz, *Astron. Astrophys.* **555**, A117 (2013), arXiv:1301.5559 [astro-ph.CO].
- [26] P. Tiwari and A. Nusser, *JCAP* **1603**, 062 (2016), arXiv:1509.02532 [astro-ph.CO].
- [27] C. J. Copi, D. Huterer, and G. D. Starkman, *Phys. Rev. D* **70**, 043515 (2004), arXiv:astro-ph/0310511 [astro-ph].
- [28] G. Katz and J. Weeks, *Phys. Rev. D* **70**, 063527 (2004), arXiv:astro-ph/0405631 [astro-ph].
- [29] M. Pinkwart, *Investigation of Cosmic Microwave Background Anomalies with Multipole Vectors*, Master's thesis, Universität Bielefeld (2016).
- [30] J. C. Maxwell, *A treatise on electricity and magnetism*, Vol. 1 (Clarendon press, 1881).
- [31] J. J. Sylvester, *Phil. Mag.* **2**, 291 (1876).
- [32] C. J. Copi, "Multipole Vector Program," <http://www.phys.cwru.edu/projects/mpvectors/> (2016-07-24).
- [33] R. u. H. D. Courant, *Methoden der Mathematischen Physik I*, 3rd ed. (Springer-Verlag Berlin).
- [34] M. R. Dennis, *Journal of Physics A Mathematical General* **37**, 9487 (2004), math-ph/0408046.
- [35] P. Schupp, *Communications in Mathematical Physics* **207**, 481 (1999), math-ph/9902017.
- [36] V. Arnold, *Journal of the Juliusz Schauder Center* **7**, 205 (1996).
- [37] M. R. Dennis, *J. Phys.* **A38**, 1653 (2005), arXiv:math-ph/0410004 [math-ph].
- [38] M. R. Dennis and K. Land, *Mon. Not. Roy. Astron. Soc.* **383**, 424 (2008), arXiv:0704.3657 [astro-ph].
- [39] E. Wigner, *Gruppentheorie und ihre Anwendung auf die Quantenmechanik der Atomspektren*, Wissenschaft (Braunschweig, Germany) (J.W. Edwards, 1931).
- [40] J. H. Hannay, *Journal of Physics A: Mathematical and General* **29**, L101 (1996).
- [41] V. Bargmann, *Communications on Pure and Applied Mathematics* **14**, 187 (1961).
- [42] http://irsa.ipac.caltech.edu/data/Planck/releaseprotect_{}/2/all-sky-maps/matrix\protect_{}cmb.html.
- [43] <http://healpix.sf.net>.
- [44] K. M. Gorski, E. Hivon, A. J. Banday, B. D. Wandelt, F. K. Hansen, M. Reinecke, and M. Bartelman, *Astrophys. J.* **622**, 759 (2005), arXiv:astro-ph/0409513 [astro-ph].
- [45] J. O. Irwin, *j-BIOMETRIKA* **19**, 225 (1927).
- [46] P. Hall, *Biometrika* **19**, 240 (1927).
- [47] L. R. Abramo, A. Bernui, I. S. Ferreira, T. Villela, and C. A. Wuensche, *Phys. Rev. D* **74**, 063506 (2006), arXiv:astro-ph/0604346 [astro-ph].
- [48] https://lambda.gsfc.nasa.gov/toolbox/tb\protect_{}coordconv.cfm.
- [49] J. B. Hough, M. Krishnapur, Y. Peres, and B. Virág, *Zeros of Gaussian Analytic Functions and Determinantal Point Processes*, University Lecture Series, Vol. 51 (American Mathematical Society, 2009).
- [50] A. Edelman and E. Kostlan, *Bulletin of the American Mathematical Society* **32**, 1 (1995).